Basin Research

IAS EAGE

Basin Research (2015) 1–20, doi: 10.1111/bre.12111

Fault-controlled fluid flow inferred from hydrothermal vents imaged in 3D seismic reflection data, offshore NW Australia

Craig Magee, Oliver B. Duffy, Kirsty Purnell, Rebecca E. Bell, Christopher A.-L. Jackson and Matthew T. Reeve

Basins Research Group (BRG), Department of Earth Science and Engineering, Imperial College, London, UK

ABSTRACT

Fluid migration pathways in the subsurface are heavily influenced by pre-existing faults. Although studies of active fluid-escape structures can provide insights into the relationships between faults and fluid flow, they cannot fully constrain the geometry of and controls on the contemporaneous subsurface fluid flow pathways. We use 3D seismic reflection data from offshore NW Australia to map 121 ancient hydrothermal vents, likely related to magmatic activity, and a normal fault array considered to form fluid pathways. The buried vents consist of craters up to 264 m deep, which host a mound of disaggregated sedimentary material up to 518 m thick. There is a correlation between vent alignment and underlying fault traces. Seismic-stratigraphic observations and fault kinematic analyses reveal that the vents were emplaced on an intra-Tithonian seabed in response to the explosive release of fluids hosted within the fault array. We speculate that during the Late Jurassic the convex-upwards morphology of the upper tip-lines of individual faults acted to channelize ascending fluids and control where fluid expulsion and vent formation occurred. This contribution highlights the usefulness of 3D seismic reflection data to constraining normal fault-controlled subsurface fluid flow.

INTRODUCTION

Rift basin architecture influences subsurface fluid flow. In particular, normal faults may represent either barriers to or conduits for fluid flow, depending on their geometry, growth history, hydraulic properties, and the nature of the displaced host stratigraphy (e.g., Yielding *et al.*, 1997; Walsh *et al.*, 1998; Ligtenberg, 2005; Cartwright *et al.*, 2007; Andresen *et al.*, 2009; Andresen, 2012). Normal fault arrays thus affect the migration of hydrothermal fluids (e.g., Hansen, 2006; Groves & Bierlein, 2007; Jackson, 2012; Giordano *et al.*, 2013; Egger *et al.*, 2014), magma (e.g., Valentine & Krogh, 2006; Gaffney *et al.*, 2007; Mazzarini, 2007; Bedard *et al.*, 2012; Magee *et al.*, 2013c) and hydrocarbons (e.g., Allan, 1989; Cartwright *et al.*, 2007). Because subsurface interactions between faults and fluids cannot be directly observed easily, examining the distribution of surficial fluid-escape structures can therefore provide crucial insights into how underlying fault arrays may influence fluid flow (e.g., Hovland *et al.*, 1994; Ligtenberg, 2005; Abebe *et al.*, 2007).

Here, we use high-quality, 3D seismic reflection data from the Exmouth Sub-basin, offshore NW Australia to analyse a suite of buried 'crater-hosted mound' structures. These crater-hosted mounds are circular to elliptical in map-view with diameters of <3.5 km. They consist of an erosive, crater base that is up to 264 m deep, and which is filled by a mound of sedimentary material up to 518 m thick. This geometry is similar to crater-hosted mounds observed elsewhere, which form in a range of geological settings in response to the expulsion of fluid at the surface (e.g., Stewart, 1999; Hansen *et al.*, 2005; Hovland *et al.*, 2005; Hansen, 2006; Andresen, 2012). In particular, the crater-hosted mounds bear a distinct resemblance to eye-shaped hydrothermal vents observed offshore Norway (e.g., Hansen, 2006). We suggest that the crater-hosted mounds analysed are ancient hydrothermal vents, perhaps related to magmatic activity, which developed on an early to middle Tithonian palaeo-seabed. Because the majority of the vents are organized into chains that are aligned subparallel to underlying normal fault traces, we employ alignment analyses and examine the growth histories of the faults to assess if, and how, the subsurface structure influenced fluid flow. Although this study is primarily concerned with hydrothermal activity, our results are broadly applicable to other forms of subsurface fluid flow and indicate that: (i) the convex-upwards morphology of fault upper tip-lines may 'capture' ascending fluids, localizing eventual hydraulic failure of the overburden; (ii) fault interactions within high-density fault arrays produce complex fluid distribution patterns; and (iii) detailed

Correspondence: Craig Magee, Basins Research Group (BRG), Department of Earth Science and Engineering, Imperial College, Prince Consort Road, London SW7 2BP, UK. E-mail: c.magee@imperial.ac.uk

© 2015 The Authors
Basin Research © 2015 John Wiley & Sons Ltd, European Association of Geoscientists & Engineers and International Association of Sedimentologists

analyses of ancient, fluid-escape structures and the contemporaneous tectono-stratigraphic and magmatic framework, imaged in 3D seismic reflection data, can provide critical insights into controls on subsurface fluid flow.

GEOLOGICAL SETTING

The Exmouth Sub-basin, located offshore NW Australia (Fig. 1a), initiated during the Early Jurassic within the North Carnarvon Basin. Formation of the Exmouth Sub-basin occurred in response to continental rifting between the Exmouth Plateau and Australia (Tindale *et al.*, 1998). Although the North Carnarvon Basin records a complex history of rifting, which extends back to the Devonian (see McClay *et al.*, 2013 and references therein), only the Pliensbachian–Callovian and Late Jurassic-to-Early Cretaceous rift phases are imaged in the 3D seismic reflection data utilized here (Figs 1b and 2) (Magee *et al.*, 2013c). Pre-Pliensbachian strata, herein referred to as 'pre-rift', are dominated by the Late Triassic to Early Jurassic, non- to shallow-marine siliciclastics of the Mungaroo and Brigadier formations (Figs 1b and 2) (Driscoll & Karner, 1998; Tindale *et al.*, 1998). Crustal extension during the Pliensbachian produced an array of vertically extensive, NE-SW striking, large normal faults with throws of up to 1 km (Fig. 1b). Overlying the 'pre-rift' strata are marine claystones of the Murat and Athol formations ('syn-rift I'), which thicken towards these faults, indicating that the faults were surface-breaking during the Early and Middle Jurassic (Figs 1b and 2) (Driscoll & Karner, 1998;

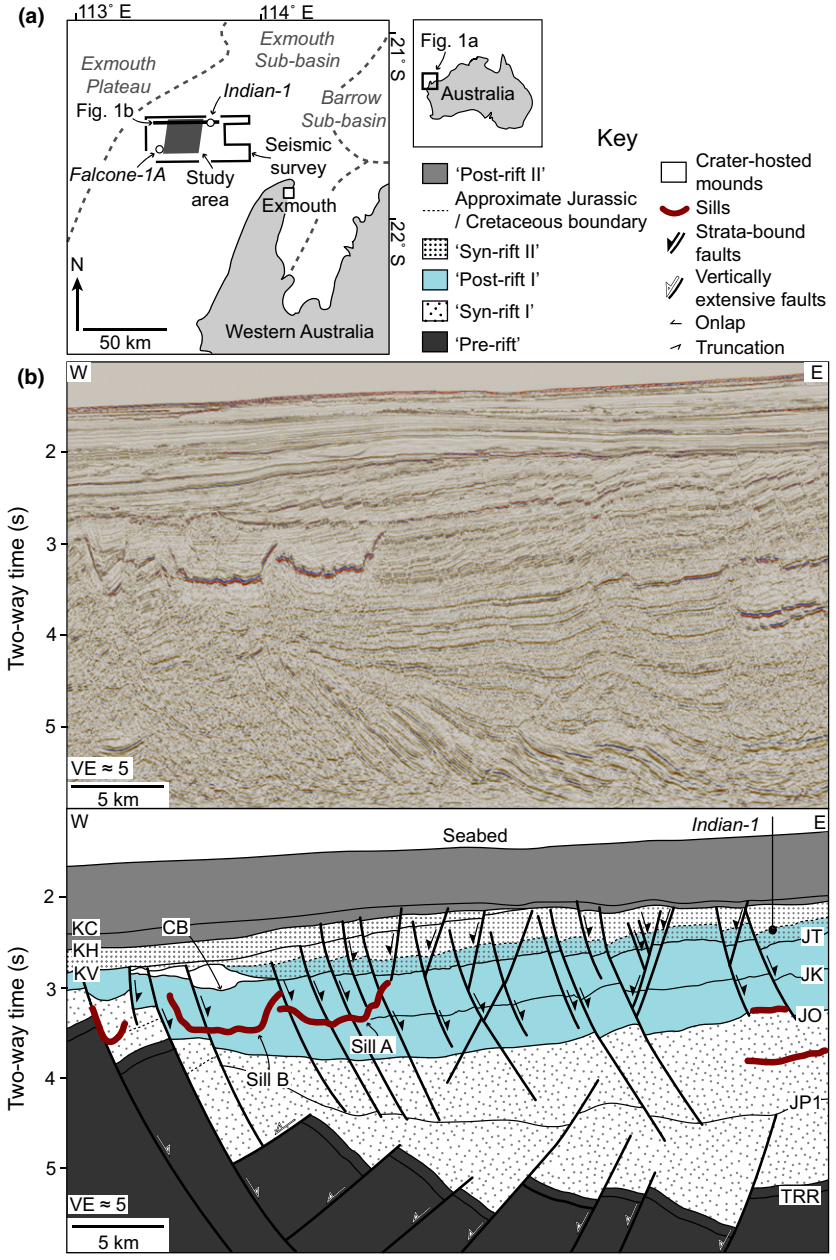

Fig. 1. (a) Location map of the 3D seismic reflection dataset and the study area offshore NW Australia. (b) Uninterpreted and interpreted seismic section highlighting the geology of the study area. Due to uncertainty in the timing of the 'post-rift I' to 'syn-rift II' transition, the ornaments applied to both are partially overlapped. See Fig. 1a for location.

© 2015 The Authors
Basin Research © 2015 John Wiley & Sons Ltd, European Association of Geoscientists & Engineers and International Association of Sedimentologists

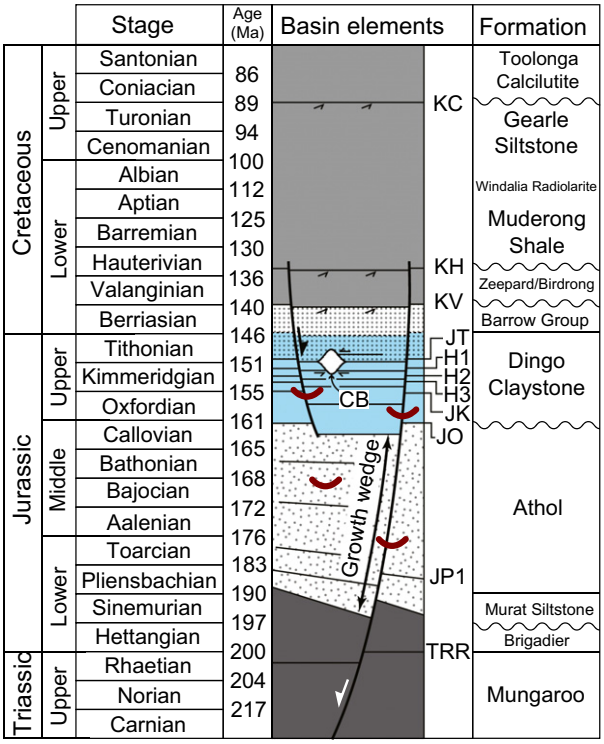

Fig. 2. Stratigraphic column identifying the key tectonic elements of the basin. See Fig. 1 for key.

Tindale *et al.*, 1998; Jitmahantakul & McClay, 2013). An ensuing period of tectonic quiescence in the Late Jurassic (i.e. 'post-rift I'; Figs 1b and 2) coincided with deposition of the Dingo Claystone, which consists of interbedded marine claystones and siltstones (Tindale *et al.*, 1998).

An influx of siliciclastic material took place in response to the onset of break-up between Australia and Greater India, resulting in deposition of the deltaic Barrow Group and Zeepard/Birdrong formations, and the onset of Late Jurassic-to-Early Cretaceous rifting ('syn-rift II') (Tindale *et al.*, 1998). This extension was accommodated by an array of NE-SW striking, low-throw (*c.* <0.1 km), conjugate normal faults that are predominantly hosted within the Dingo Claystone (Figs 1b and 2) (Jitmahantakul & McClay, 2013; Magee *et al.*, 2013c). The exact timing of 'syn-rift II' faulting is poorly constrained (Figs 1b and 2), with previous studies suggesting faulting initiated in either the early Tithonian (Driscoll & Karner, 1998; Mihut & Müller, 1998), early Berriasian (Tindale *et al.*, 1998) or early Valanginian (Rey *et al.*, 2008). In contrast, Jitmahantakul & McClay (2013) proposed that the conjugate faults developed during the late Berriasian or early Valanginian in response to thermal subsidence. A clastic sequence, which includes the Muderong Shale, Windalia Radiolarite and the Gearle Siltstone, as well as younger carbonate rocks of the Toolonga Calcilutite, form the 'post-rift II' succession (Figs 1b and 2) (Tindale *et al.*, 1998).

The Dingo Claystone and Athol Formation within the Exmouth Sub-basin host several igneous intrusions (Figs 1b and 2) (Mihut & Müller, 1998; Jitmahantakul & McClay, 2013; Magee *et al.*, 2013a,c). On seismic reflection data, these intrusions manifest as very high-amplitude anomalies that characterize a downward increase in acoustic impedance and have a strata-concordant or saucer-shaped morphology (e.g., Fig. 1b) (Symonds *et al.*, 1998; Magee *et al.*, 2013a). These characteristics are similar to sills drilled in other sedimentary basins (e.g., the Faroe-Shetland Basin; Smallwood & Maresh, 2002). A few basaltic sills have been penetrated by wells within the North Carnarvon Basin (e.g., the Yardie East-1 borehole; Mihut & Müller, 1998).

DATASET AND WORKFLOW

This study uses a time-migrated, zero-phase, 3D seismic reflection survey covering an area of 1200 km^2 (Fig. 1a). The inlines and cross-lines are oriented E-W and N-S, with spacings of 14.06 m and 12.5 m, respectively. These data are displayed with a reverse polarity, such that a downward increase in acoustic impedance corresponds to a negative amplitude (blue) reflection and a downward decrease in acoustic impedance is represented by a positive amplitude (red) reflection. The 630 km^2 study area of interest (Fig. 1a) has an average water depth of 1.4 km.

Biostratigraphic data from the Falcone-1A and Indian-1 wells were used to constrain relative horizon ages down to the Late Triassic. To depth-convert relevant measurements, the interval velocities for packages of sedimentary strata above the base Oxfordian (horizon JO; see Figs 1 and 2) were obtained directly from the Falcone-1A and Indian-1 wells (Fig. 3). The Late Triassic to Early Jurassic strata are only penetrated on a footwall high by Falcone-1A. Measurements from the 'pre-rift' and 'syn-rift I' successions were thus depth-converted using extrapolated interval velocities, ranging from *c.* 3.5–4.1 km s^{-1} (Fig. 3), to avoid complications associated with footwall uplift. The dominant frequency of the seismic data in the vicinity of the crater-hosted mounds is 40 Hz, which together with an interval velocity of 2.2 km s^{-1} implies that the data locally has a limit of separability of 14 m and a limit of visibility of 2 m (*sensu* Brown, 2004). The limits of separability and visibility increase with depth, up to 52 m and 7 m, respectively, where seismic velocities reach 4.1 km s^{-1} and the dominant frequency is 20 Hz. Igneous intrusions within the dataset have a dominant frequency of 20 Hz and are assumed to have interval velocities of 5.6 km s^{-1} (Skogly, 1998), indicating that they have a limit of separability of 70 m and a limit of visibility of 10 m.

To evaluate the origin of the crater-hosted mounds, it is important to first determine the tectono-stratigraphic framework for the basin by mapping seismic horizons and constraining fault array architecture. Igneous intrusions, which may instigate and/or influence fluid flow (e.g., Jamtveit *et al.*, 2004; Hansen, 2006; Svensen *et al.*, 2006; Holford *et al.*, 2012), located within the study area were also mapped. Constructing this framework provides the context for our quantitative analysis of the crater-hosted mounds, allowing their spatial and temporal evolution to

© 2015 The Authors
Basin Research © 2015 John Wiley & Sons Ltd, European Association of Geoscientists & Engineers and International Association of Sedimentologists

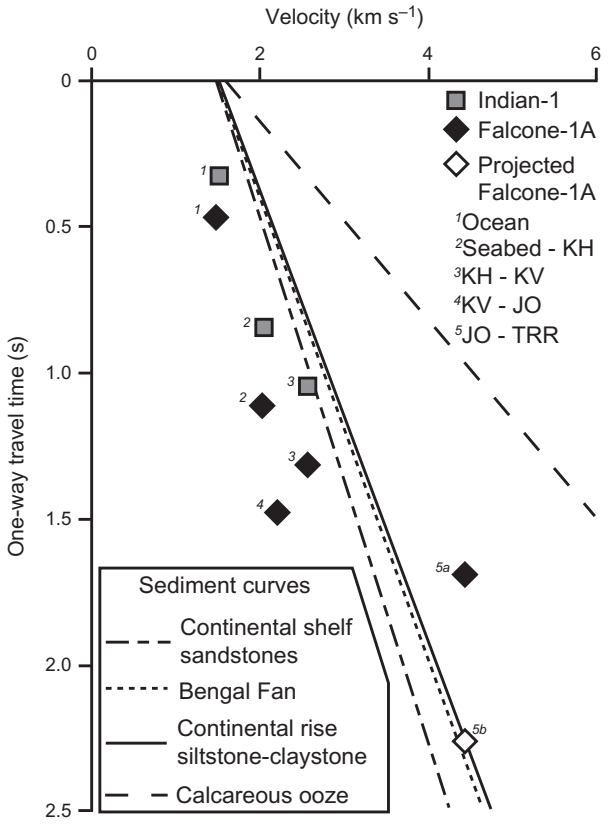

Fig. 3. Seismic velocity data obtained from the Falcone-1A and Indian-1 wells plotted against the one-way travel time mid-point for a series of stratigraphic intervals. Velocity-depth profiles of a range of sedimentary rocks are provided for comparison after (Hamilton *et al.*, 1977; Hamilton, 1985).

be assessed and compared to previously described fluid-escape features. To date the crater-hosted mounds, igneous intrusions and faults, we analyse seismic-stratigraphic relationships and construct fault throw vs. stratigraphic age plots, which allow fault nucleation depths and thus relative ages to be inferred (e.g., Mansfield & Cartwright, 1996; Hongxing & Anderson, 2007; Baudon & Cartwright, 2008; Jackson & Rotevatn, 2013). We also conducted a statistical alignment analysis of the crater-hosted mounds and faults to evaluate their spatial relationship. The techniques employed allow the origin and evolution of the crater-hosted mounds to be constrained, providing insights into the controls on their distribution. Further detail on each methodology employed is provided at the start of each relevant results section.

TECTONO-STRATIGRAPHIC AND MAGMATIC FRAMEWORK

To define the local stratigraphic architecture, 11 major seismic horizons have been mapped at least every 25 inlines and cross-lines (Figs 1b, 2, 4 and 5). Due to uncertainties regarding the precise position and age of the 'post-rift I' and 'syn-rift II' transition (Driscoll & Karner, 1998; Mihut & Müller, 1998; Tindale *et al.*, 1998; Rey *et al.*, 2008), this boundary is only mapped locally (e.g., Figs 1b, 2 and 4). Additionally, 383 faults have been mapped every *c.* 140 m along-strike and fault traces extracted at different stratigraphic levels (e.g., Fig. 5). Two fault arrays are distinguished based on their height and stratal position (Figs 1b and 4): (i) 'vertically extensive' describes faults that displace Triassic strata and commonly extend up into the Upper Jurassic succession; and (ii) 'strata-bound' pertains to faults primarily restricted to the Upper Jurassic Dingo Claystone. Overall, there is little variation in mean fault strike (013–193°), with approximately 52% of the faults dipping ESE and 48% dipping WNW (Fig. 5). The west-dipping faults (30–70° with a mean of 46°) are commonly steeper than the east-dipping faults (19–58° and with a mean of 38°). Two-way time (TWT) thickness maps were generated between the mapped horizons to infer fault-controlled subsidence patterns (Fig. 6). Four sills, which may in some way be related to the crater-hosted mounds, are also mapped.

Prerift and Syn-rift I

The 'syn-rift I' sequence, bounded at the top by the base Oxfordian horizon (JO), shows stratal wedges that diverge towards vertically extensive faults (e.g., Figs 1b and 6). At the structural level of the near top Triassic horizon (TRR), these vertically extensive faults are predominantly east-dipping and up to 15 km long, with typical across-strike fault spacings of 0.5–5 km and throws of up to 1 km (Figs 1b and 5a). The spacing of faults at the base Oxfordian structural level is <2 km, principally because the horizon is cross-cut by numerous strata-bound faults that typically tip out at the near base Pliensbachian horizon (JP1) and do not extend down into Triassic strata (Figs 1b, 4 and 5b). Fault strike changes from N-S in the west to NE-SW in the east, and the faults have relatively modest throws of <150 m (Fig. 5b).

Post-rift I, Syn-rift II and Post-rift II

Seven horizons have been mapped within 'post-rift I', including the base Kimmeridgian (JK), three intra-Kimmeridgian horizons (H1–H3) and a horizon within the early to middle Tithonian age (JT) (Figs 1b, 2, 4 and 5). The intra-Tithonian horizon is truncated by the intra-Valanginian unconformity (KV) (Fig. 1b). A two-way time thickness map between the intra-Valanginian and intra-Tithonian horizons highlights several sub-circular zones of locally thinned strata, organized into a N-S oriented linear chain, that are superimposed onto the overall north-easterly thickening trend (Fig. 6c). The strata-bound faults developed between the base Oxfordian and intra-Valanginian horizons generally strike NE-SW and the fault density is highest at the structural level of H3 (i.e. within the Kimmeridgian; Fig. 5). A few faults extend above the intra-Hauterivian (KH) horizon but

© 2015 The Authors
Basin Research © 2015 John Wiley & Sons Ltd, European Association of Geoscientists & Engineers and International Association of Sedimentologists

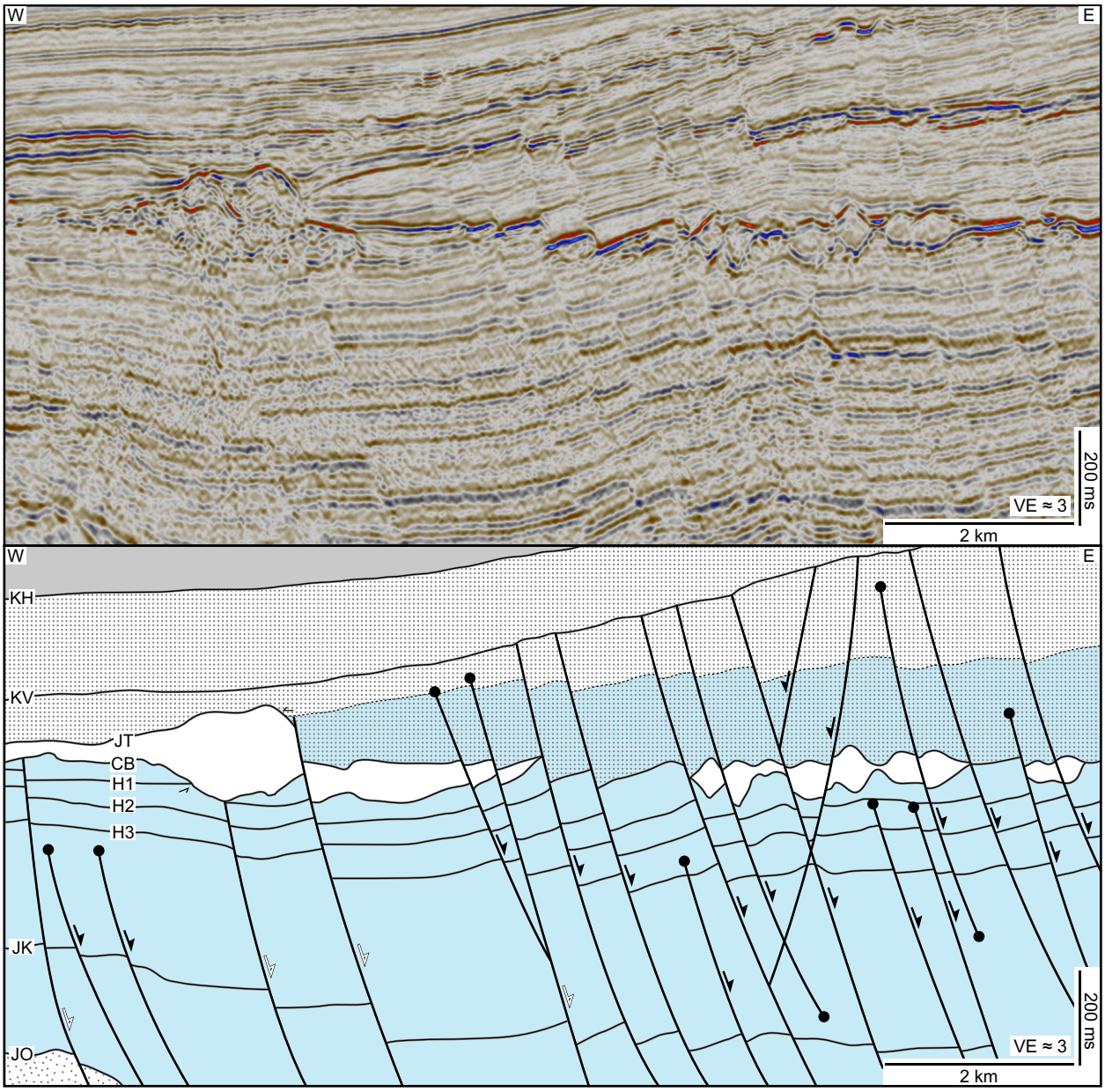

Fig. 4. Uninterpreted and interpreted seismic section highlighting the geology in the vicinity of the crater-hosted mounds. See Fig. 1 for key and Fig. 5a and for location.

none displace the base Cenomanian (KC) horizon (Fig. 1b).

Igneous intrusions

Magmatic activity commonly instigates hydrothermal fluid flow and may produce structures similar to the crater-hosted mounds described here (Jamtveit *et al.*, 2004; Svensen *et al.*, 2006). It is thus important to constrain location and structure of the four intrusions (A–D) identified within the study area. These intrusions are characterized by very high-amplitude seismic reflections and correspond to a downward increase in acoustic impedance (Fig. 7). The sills are primarily hosted within the Dingo Claystone between the H2 intra-Kimmeridgian horizon and the base Oxfordian. The sills typically have a saucer-shaped morphology (Figs 1b and 7). Aside from portions of the Sill B and Sill D inclined limbs that are parallel to and coincident with a fault plane, Fig. 7 shows that the intrusions either directly cross-cut faults or display a small downward step into fault hanging walls. Similar interactions are observed between Sill A and surrounding faults (see Magee *et al.*, 2013c).

CRATER-HOSTED MOUNDS

In this section, we describe the geometry, seismic expression and distribution of the crater-hosted mounds in relation to the tectono-stratigraphic and magmatic

© 2015 The Authors
Basin Research © 2015 John Wiley & Sons Ltd, European Association of Geoscientists & Engineers and International Association of Sedimentologists

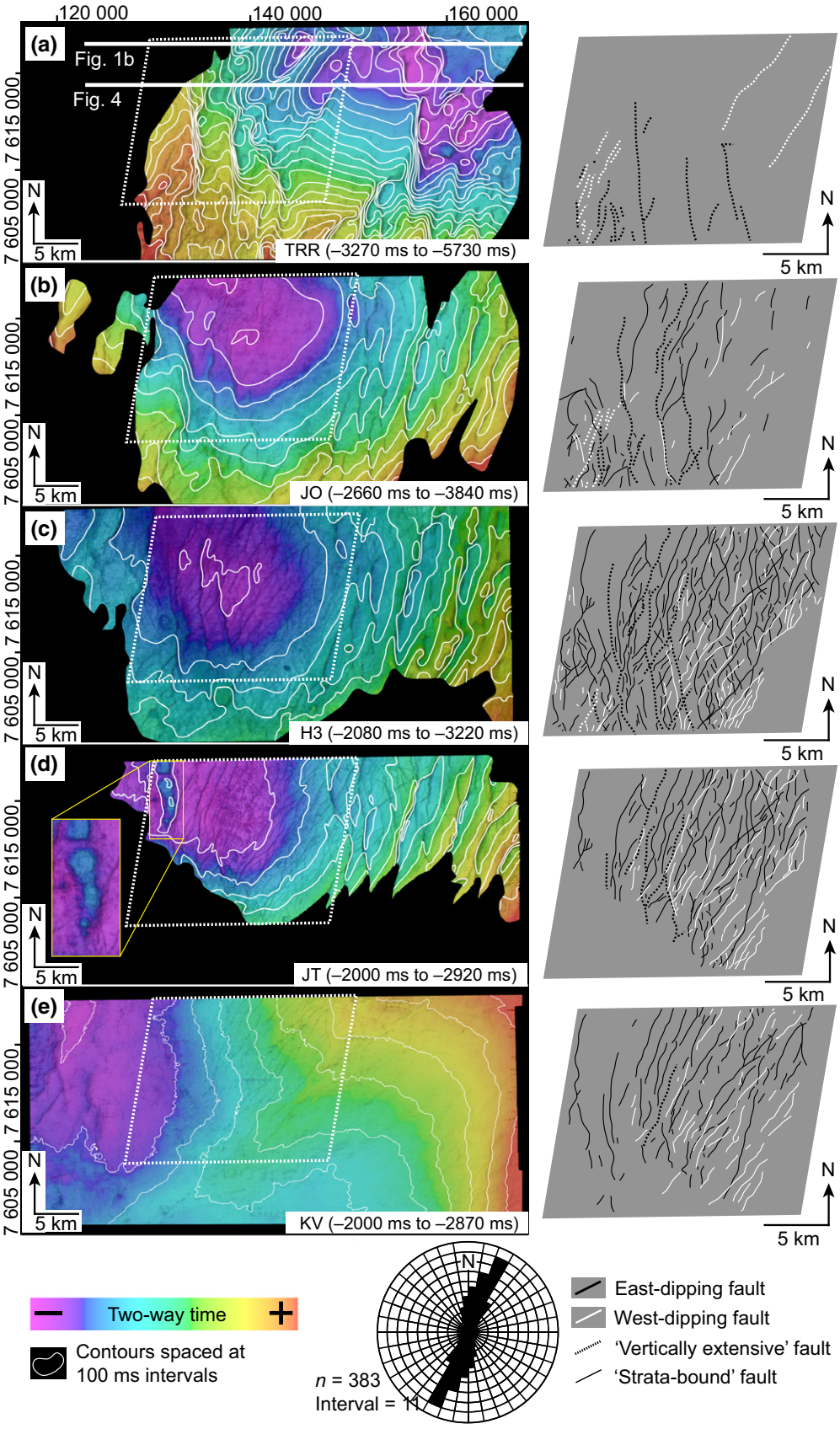

Fig. 5. Time-structure maps: (a) the near top Triassic – TRR; (b) the base Oxfordian – JO; (c) and intra-Kimmeridgian horizon – H3; (d) an early to middle Tithonian horizon – JT and (e) the Hauterivian unconformity – KH. Maps of horizon and fault intersections within the study area and a rose diagram depicting the average strikes of the entire fault population are also provided. The co-ordinates used correspond to WGS 1984 UTM Zone 50S.

© 2015 The Authors
Basin Research © 2015 John Wiley & Sons Ltd, European Association of Geoscientists & Engineers and International Association of Sedimentologists

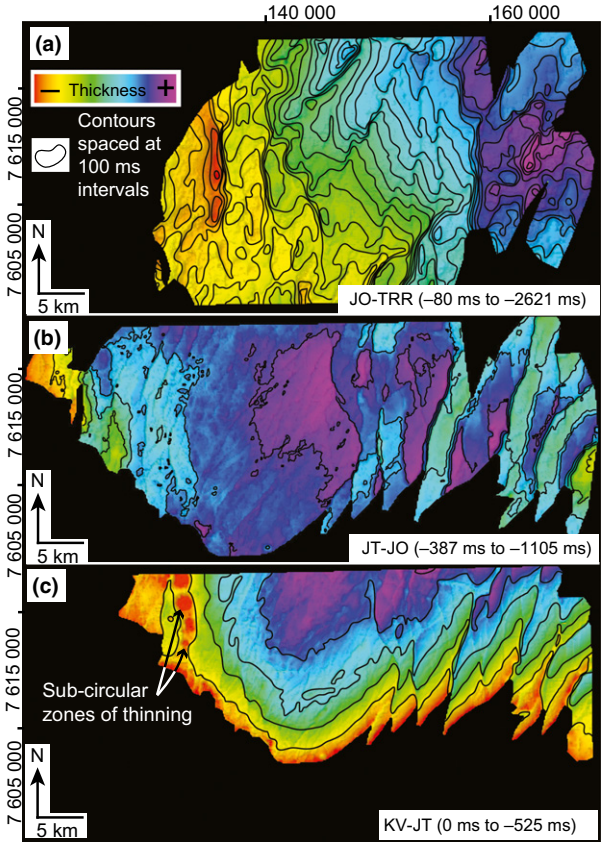

Fig. 6. Maps showing spatial variations in the vertical thickness (in TWT) of the strata between the base Oxfordian and near top Triassic (JO-TRR), the intra-Tithonain and base Oxfordian (JT-JO), and the intra-Valanginian unconformity and intra-Tithonian horizon (KV-JT) mapped. For clarity, fault polygons have been omitted. The co-ordinates used correspond to WGS 1984 UTM Zone 50S. (a) The Early and Middle Jurassic strata of 'syn-rift I' thins westwards (see also Fig. 1b). (b) Upper Jurassic strata between the base Oxfordian and intra-Tithonian horizons show thickness variations primarily associated with fault blocks, although no patterns attributable to syn-kinematic sedimentation (i.e. thickening towards faults) are apparent. (c) The uppermost Jurassic and Early Cretaceous succession gradually thickens towards a central depocentre in the north of the survey. Several sub-circular zones demarcated by abrupt thinning, and aligned along a N-S orientation, are observed to the west of the mapped area.

framework outlined above. This facilitates comparison to previously described fluid-escape features, allowing the origin and evolution of the crater-hosted mounds to be constrained.

Morphology and seismic expression

The top of the crater-hosted mounds coincides with the early to middle Tithonian horizon, which locally displays a relief of up to 254 m (Figs 1b, 4, 7, 8a and b). The mounds are onlapped by overlying reflections (Figs 7a and 8a). Minor dome-shaped folds with amplitudes *c.* <15 m are occasionally developed above the mounds in overlying strata (e.g., Fig. 8a). The base of the crater-hosted mounds (CB; Figs 1b and 4), defines numerous craters that are up to 264 m deep and truncate underlying reflections (Fig 8a and c). The underlying and overlying strata display a similar seismic facies character to that of the crater-hosted mounds and typically belong to the Upper Jurassic Dingo Claystone (Figs 1b, 4, 7 and 8a). Some of the larger crater-hosted mounds in the west of the study area are onlapped by 'syn-rift II' strata or are truncated by the intra-Valanginian unconformity (Figs 1b, 4 and 7).

Thickness variations between the intra-Tithonian horizon and the base of the craters allow us to map 121 individual crater-hosted mounds, which are occasionally encompassed by an apron of material at the same stratigraphic level (Fig. 8d). Some areas of reduced thickness correspond to cross-cutting normal faults, which primarily displace the intra-Tithonian horizon in zones adjacent to or along the flanks of crater-hosted mounds (e.g., Figs 4 and 8a). Between the intra-Tithonian horizon and the crater base, reflections are typically of low-amplitude and chaotic (e.g., Fig. 4) although continuous reflections, which are conformable to the intra-Tithonian horizon and downlap onto the crater base horizon, can be discerned within some crater-hosted mounds (e.g., Figs 7a and 8a). No resolvable sub-vertical, linear zones of seismic disturbance are observed below or above the crater-hosted mounds (Figs 4, 7 and 8a).

Geometry

Due to the complex map-view morphologies of the crater-hosted mounds, a map of their outlines was exported into the ImageJ analysis software (Rasband, 1997) to generate best-fit ellipses (Fig. 8e). These best-fit ellipses were used to determine the centroid position, as well as the length and azimuth of the long and short axes for each crater-hosted mound (Figs 8e and 9a). Crater-hosted mounds with axial ratios >1.2 are described as being 'elongate' whereas those with values <1.2 are described as 'circular' (Paulsen & Wilson, 2010). Within the individual crater-hosted mound boundaries, time-structure maps of the intra-Tithonian horizon and the crater base horizon were created to derive the location of the maximum crater depths and mound heights. Because the location of the maximum mound height does not always directly overlie the position of maximum crater depth (e.g., Fig. 9a), the maximum thickness of each crater-hosted mound was obtained from individually generated intra-Tithonian horizon to crater base TWT thickness maps. Volumes for the mounds and craters were calculated from their area and height/depth, assuming that the mounds and craters are divided by a datum parallel to the regional trend of the intra-Tithonian horizon (Fig. 9a) and that they have a simple conical geometry. As one crater-hosted mound extends beyond the limit of the seismic survey (Fig. 8e), it has not been incorporated into the statistical analysis of the mound and crater parameters. Four crater-

© 2015 The Authors
Basin Research © 2015 John Wiley & Sons Ltd, European Association of Geoscientists & Engineers and International Association of Sedimentologists

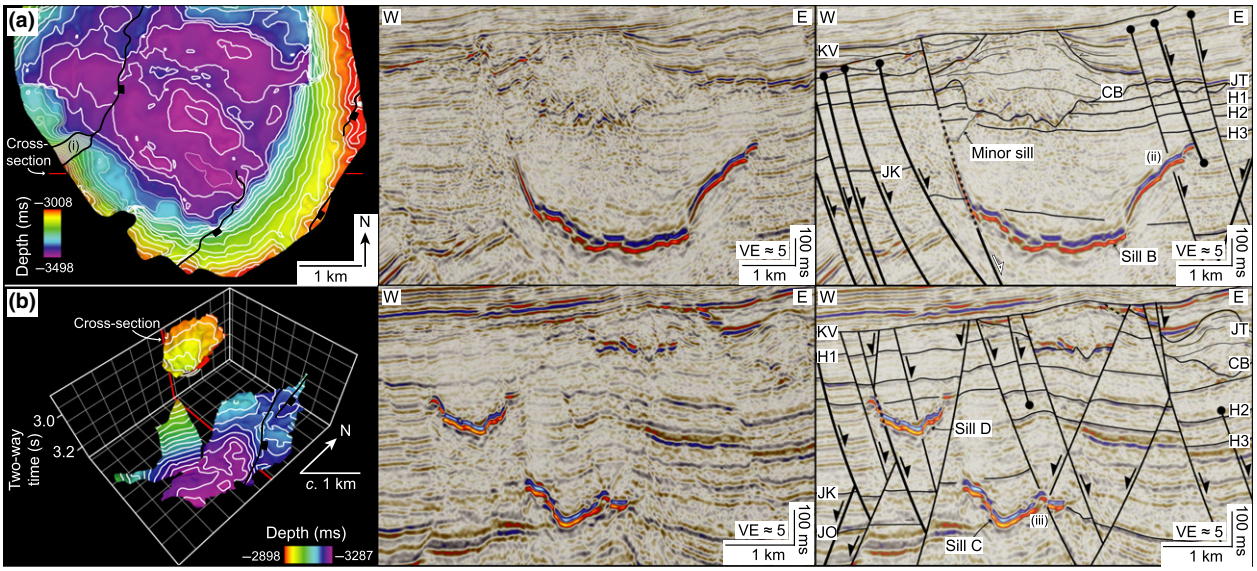

Fig. 7. (a) Time-structure map of and interpreted seismic section through Sill B. The area where the western limb of Sill B coincides with the fault plane is highlighted on the time-structure map (i). Internal reflections observed in the overlying crater-hosted mound are highlighted. Contour intervals (white lines) equal 30 ms. (b) 3D time-structure map and seismic section showing the geometry and position of sills C and D. Where a sill cross-cuts a fault with no offset (ii) or displays a downward step into the hanging wall (iii) are highlighted. Contour intervals (white lines) equal 15 ms. See Fig. 10a for location. Uninterpreted seismic sections are provided in the supplementary data.

hosted mound are truncated by the intra-Valanginian unconformity (e.g., Fig. 7a); the mound height measurements of these are therefore minimum values. Structural measurements for all 121 crater-hosted mounds are presented in the supplementary data.

The crater-hosted mounds range in area from 0.35 to 4.93 km^2 and have long axes between 0.27 and 3.35 km. The calculated axial ratios, which range from 1.04 to 4.20, indicate that 84% of the crater-hosted mounds are 'elongated' and 16% are 'circular'. The rose diagram in Fig. 8e shows that, although the crater-hosted mound long axis orientation is variable, three major trends can be defined: NE-SW (10%); N-S (28%); and NW-SE (17%). There is a strong positive correlation between crater depths, which range from 22 to 264 m, and mound heights (8–254 m). On average, the crater depth of individual crater-hosted mounds is 22% greater than the mound height (Fig. 9b). A moderate, positive correlation exists between the crater depth or mound height, and the respective diameter of individual crater-hosted mounds (Fig. 9c). The maximum thickness and volume of the crater-hosted mounds range from 43 to 372 m and 0.03 to 4.31 km^3, respectively. The craters and mounds have mean volumes of 0.16 km^3 and 0.14 km^3. Total volumes of all craters and mounds are *c*. 19 km^3 and *c*. 17 km^3, respectively.

Distribution

The distribution of fluid flow-related structures is related to the processes that control their formation and evolution (e.g., Bonini & Mazzarini, 2010; Paulsen & Wilson, 2010; Le Corvec *et al.*, 2013). It is apparent from Fig. 8e that the crater-hosted mounds occur in three broadly linear belts; Groups 1 and 2 are oriented 018–198° and are sub-parallel to the average fault strike (see Fig. 4), whereas Group 3 is oriented 036–216°. Within these groups and particularly within Group 2, numerous chains of approximately five or fewer crater-hosted mounds can be recognized that are sub-parallel to individual fault traces (Fig. 10). Relative to fault traces defined at the intra-Tithonian horizon (Fig. 5d), the majority of maximum crater depth positions are offset into fault hanging walls by *c*. 50–100 m (Fig. 10a). In contrast, Fig. 10b and c reveal that the maximum crater depth positions typically directly overlie fault traces occurring along the H3 intra-Kimmeridgian horizon. There is little spatial correlation between the crater-hosted mounds and the mapped sills; i.e. only 19 crater-hosted mounds occur either directly above the sills or within 100 m of their seismically resolved lateral terminations (Fig. 10a).

To quantify the observed trends and determine whether they record information on the primary controls of crater-hosted mound distribution, we applied the technique of Paulsen & Wilson (2010) with the aim of statistically testing the spatial correlations identified. This method allows 'alignment reliability' to be assessed, providing a measure of confidence in the spatial relationship between the crater-hosted mounds and faults (see Bonini & Mazzarini, 2010; Paulsen & Wilson, 2010; Le Corvec *et al.*, 2013; Isola *et al.*, 2014). For Groups 1–3, orthogonal linear regression best-fit lines were calculated from the crater-hosted mound centroid positions (Fig. 9a) (see Paulsen & Wilson, 2010). Ten fault traces (Faults *a–j*) from H3 within the Kimmeridgian, which underlie chains

© 2015 The Authors
Basin Research © 2015 John Wiley & Sons Ltd, European Association of Geoscientists & Engineers and International Association of Sedimentologists

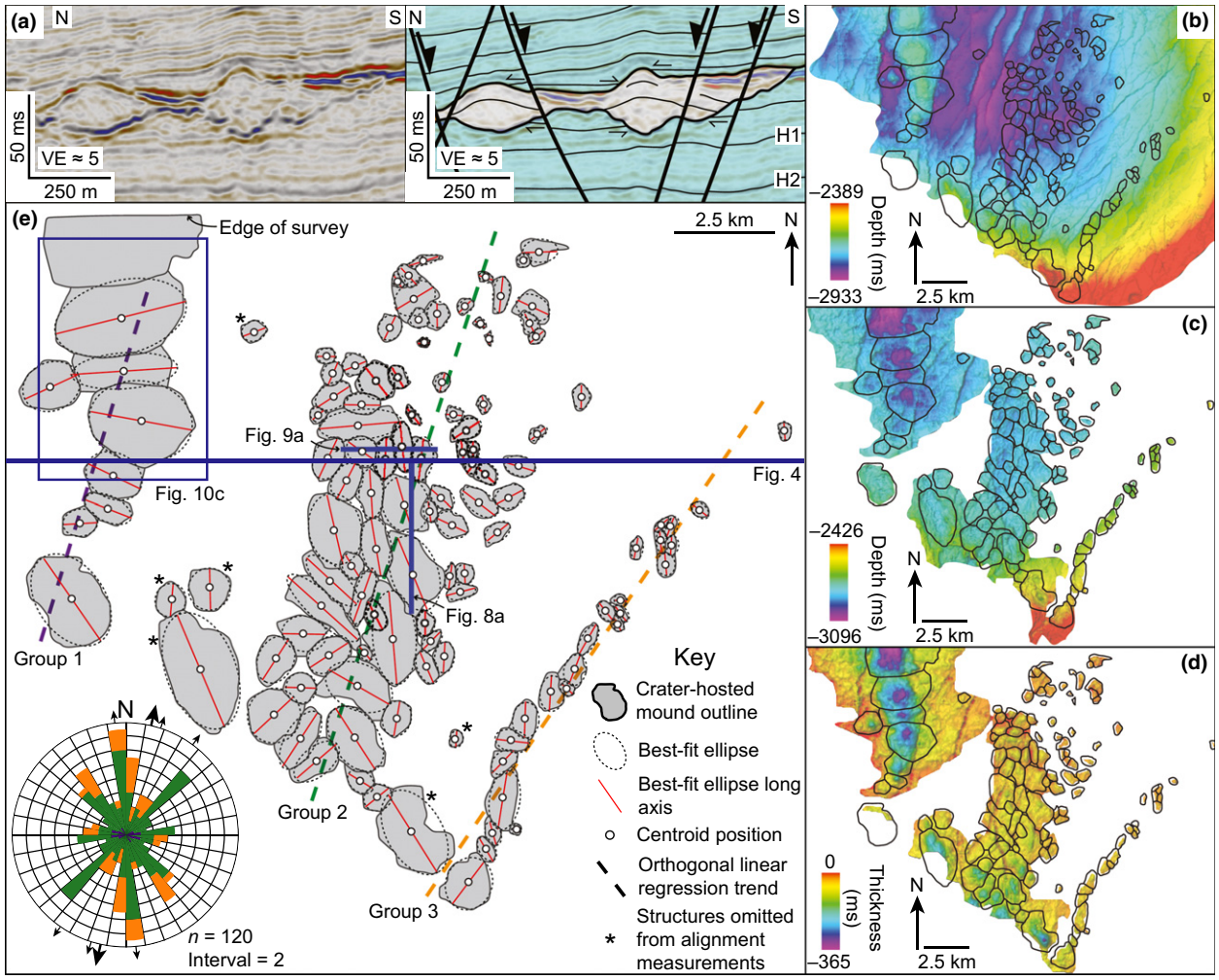

Fig. 8. (a) Uninterpreted and interpreted seismic section of two crater-hosted mounds. See Fig. 1 for key and Fig. 8e for location. (b and c) Time-structure maps of the intra-Tithonian horizon and crater base horizon, respectively, highlighting the mapped crater-hosted mounds. (d) TWT thickness map between the intra-Tithonian and crater base used to determine the outline of individual crater-hosted mounds. Contours are omitted for clarity. (e) Map of the defined crater-hosted mounds. Due to their complex map-view morphology, best-fit ellipses were calculated and used to establish the centroid position, long axis length and long axis azimuth (see rose diagram inset) of each crater-hosted mound. Where adjacent crater-hosted mounds impinge and merge together, the mid-point of the intervening trough was used to define individual crater-hosted mound boundaries. Inset: The rose diagram depicts the long axis azimuth of the crater-hosted mounds within Groups 1 (purple), 2 (green) and 3 (orange). The small arrows indicate the azimuth of the three groups whilst the large arrow is the average trend of the mapped faults.

of maximum crater depth positions, were also selected (Fig. 10b) and in these cases it was assumed that the fault traces correspond to a best-fit line. The following parameters were subsequently measured (Fig. 9a): (i) the orthogonal distance to each associated centroid point for Groups 1–3 or maximum crater depth position for Faults *a–j* from the best fit-line; (ii) the nearest neighbour spacing of the crater-hosted mounds and (iii) the angular deviation (θ) between ellipse long axes and the azimuth of the best-fit lines or fault traces was also calculated. To constrain the reliability of any spatial correlation, Bonini & Mazzarini (2010) advocated using the 'alignment length', i.e. the distance along the best-fit line (or fault trace) between the two structures which are furthest apart, to scale these measurements and compare them to predefined criteria (Table 1). As the faults analysed extend along strike beyond associated crater-hosted mound distributions (Fig. 10b), we also used the seismically resolved 'fault trace length' as a threshold to test its effect on reliability. Table 1 highlights the grading system applied to determine the reliability trends and is based upon Paulsen & Wilson (2010) and Bonini & Mazzarini (2010); 'A' describes a strong spatial correlation whereas 'D' implies that the observed trend is not statistically valid. Both average values and standard deviations of the three parameters measured are used to constrain the reliability (Table 1). This is because they provide insights into the actual relationships of the crater-hosted mounds to the best-fit line and estimates of the homogeneity in the observed trends (Bonini & Mazzarini, 2010). For each

© 2015 The Authors
Basin Research © 2015 John Wiley & Sons Ltd, European Association of Geoscientists & Engineers and International Association of Sedimentologists

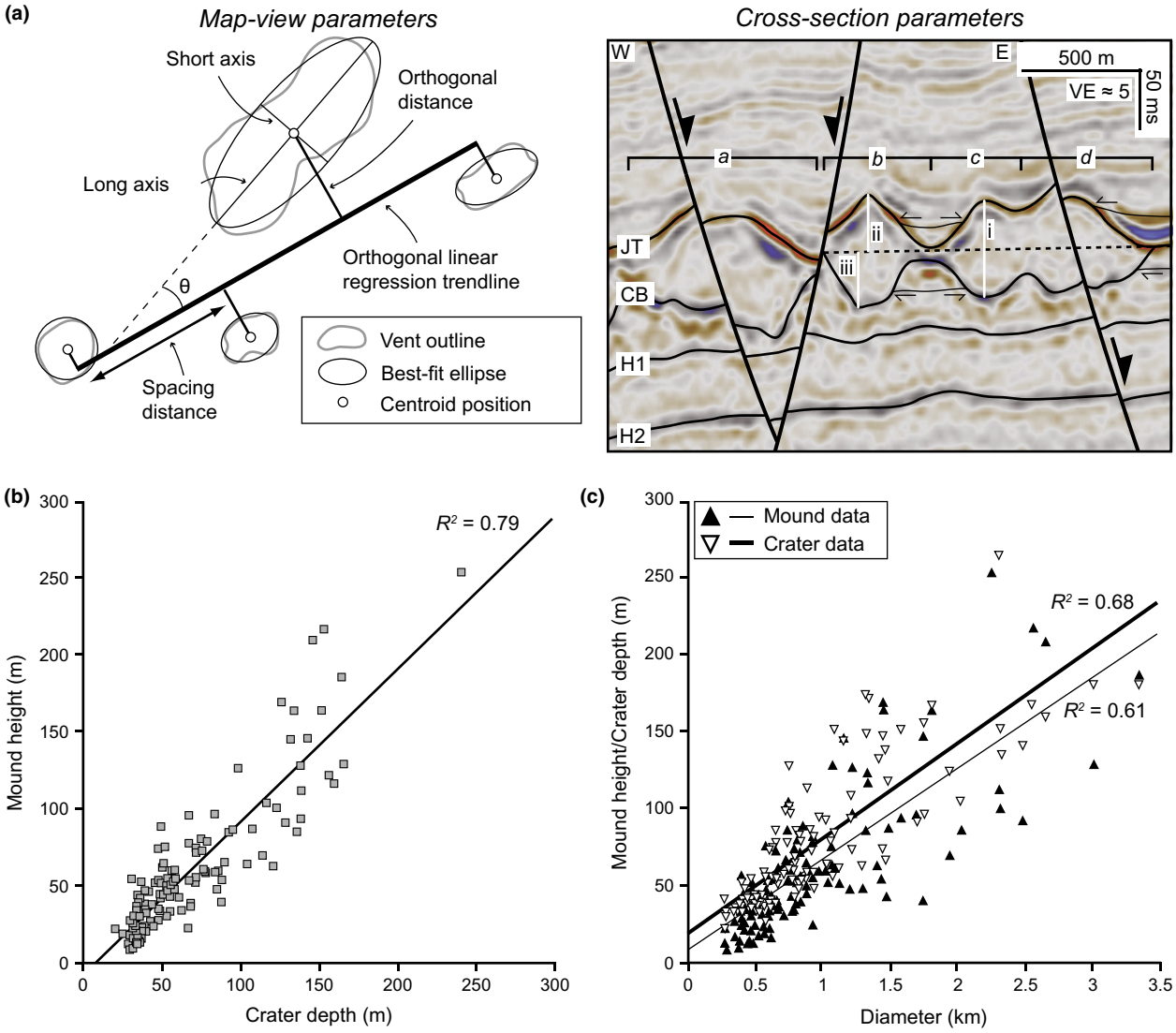

Fig. 9. (a) Schematic diagram of the map-view parameters measured (Paulsen & Wilson, 2010). The interpreted seismic section shows four crater-hosted mounds (*a–d*) and highlights how the maximum thickness (i) does not necessarily correlate spatially to the maximum mound height (ii) or crater depth (iii). The crater depth and mound height are measured from the maximum depth or summit relative to a datum (dashed line) corresponding to the regional extrapolation of JT intra-Tithonian horizon. Onlap and truncational seismic-stratigraphic relationships are also indicated. See Fig. 8e for location. An uninterpreted seismic section is provided in the supplementary data. (b) Plot of maximum crater depth against maximum mound height. (c) Diameter of the crater-hosted mound plotted against respective crater depth and mound height.

alignment trend, the lowest reliability grade returned for any of the parameters measured is used to describe the statistical validity of the correlation (Paulsen & Wilson, 2010).

Crater-hosted mounds assigned to Groups 1 and 3 are distributed relatively closely to the NE-SW trend (Fig. 8e), which is reflected in their low average orthogonal distances (570 m and 330 m respectively) (Fig. 11a; Table 2). Conversely, the clustered distribution of the Group 2 crater-hosted mounds (Fig. 8e) have an average orthogonal distance of 1237 m and a lower average vent spacing of 168 m compared to Groups 1 and 3, which have spacings of 1067 m and 586 m, respectively (Fig. 11b; Table 2). The angular deviation of Groups 1, 2 and 3 is 68.9°, 41.5° and 41.3°, respectively, (Table 2). Figure 11 and Table 2 indicate that the overall reliability grades of Groups 1–3 are low and ranges from 'C–D'.

For each of the fault trace and crater-hosted mound alignments analysed (Faults *a–j*), the average distance and spacing of the crater-hosted mounds are smaller, with ranges of 64–269 m and 250–1648 m, respectively (Table 2), compared to the broad Group 1–3 trend data (Fig. 11a). There is, however, a poor correlation between local fault strike and the orientation of the crater-hosted mound long axes, with angular deviations for Faults *a*, *b* and *d–i* ranging from 31 to 63° (Table 2). Both Faults *c* and *j* display angular deviations <30° (Table 2).

© 2015 The Authors
Basin Research © 2015 John Wiley & Sons Ltd, European Association of Geoscientists & Engineers and International Association of Sedimentologists

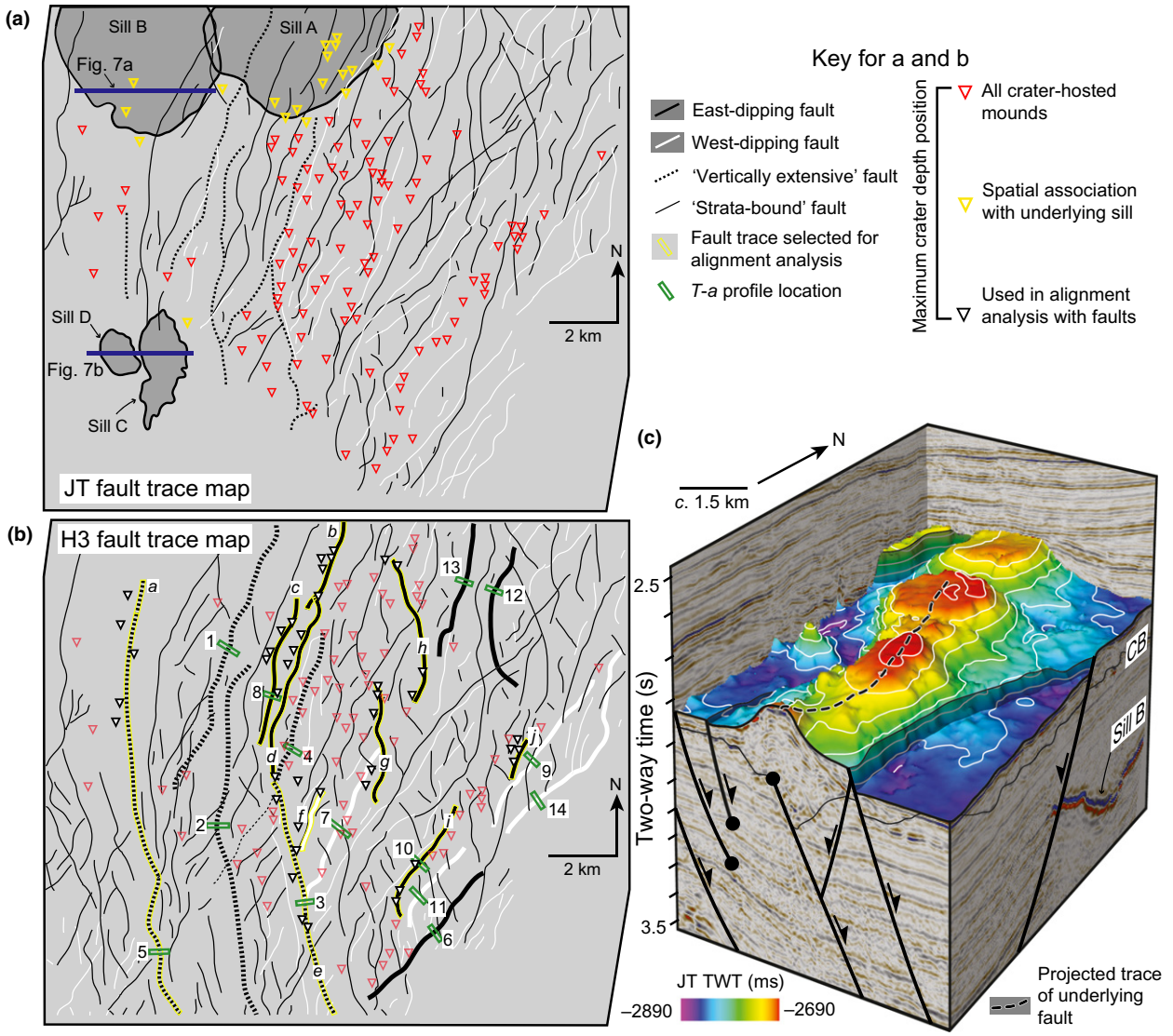

Fig. 10. (a) Fault traces along the intra-Tithonian horizon highlighting the outline of the mapped sills and the maximum crater depth positions. (b) Map depicting fault traces on the H3 intra-Kimmeridgian horizon to highlight those used in the fault throw and crater-hosted mound alignment analyses. The numbers indicate Faults 1–14 and the letters correspond to Faults *a*–*j*. The maximum crater depth positions for the crater-hosted mounds are also shown. (c) 3D block view of a chain of crater-hosted mounds elongated along a fault. See Fig. 8e for location (viewed from the south-east).

Table 1. Alignment reliability grade criteria

		Distance from best-fit line		Crater-hosted mound spacing		
Reliability grade	No. of structures	Average (m)	Standard deviation (m)	Average (m)	Standard deviation (m)	Average angular deviation (°)
A	>5	<0.020 L	<0.020 L	<0.10 L	<0.10 L	≤30
B	>4	<0.020 L	<0.020 L	<0.12 L	<0.12 L	≤35
C	>3	<0.025 L	<0.025 L	<0.15 L	<0.15 L	≤40
D	>2	No limit	No limit	No limit	No limit	>40

'L' is equal to the alignment length or fault trace.

Depending on whether these measurements are scaled using alignment length or the resolved fault length, reliability grades are either all 'D' or a mixture of 'A' (40%), 'C' (10%) and 'D' (50%)', respectively (Fig. 11; Table 2).

Evolution and classification of the crater-hosted mounds

The observation that underlying seismic reflections are truncated by the craters (Figs 1b, 4, 7a and 8a), suggest

© 2015 The Authors
Basin Research © 2015 John Wiley & Sons Ltd, European Association of Geoscientists & Engineers and International Association of Sedimentologists

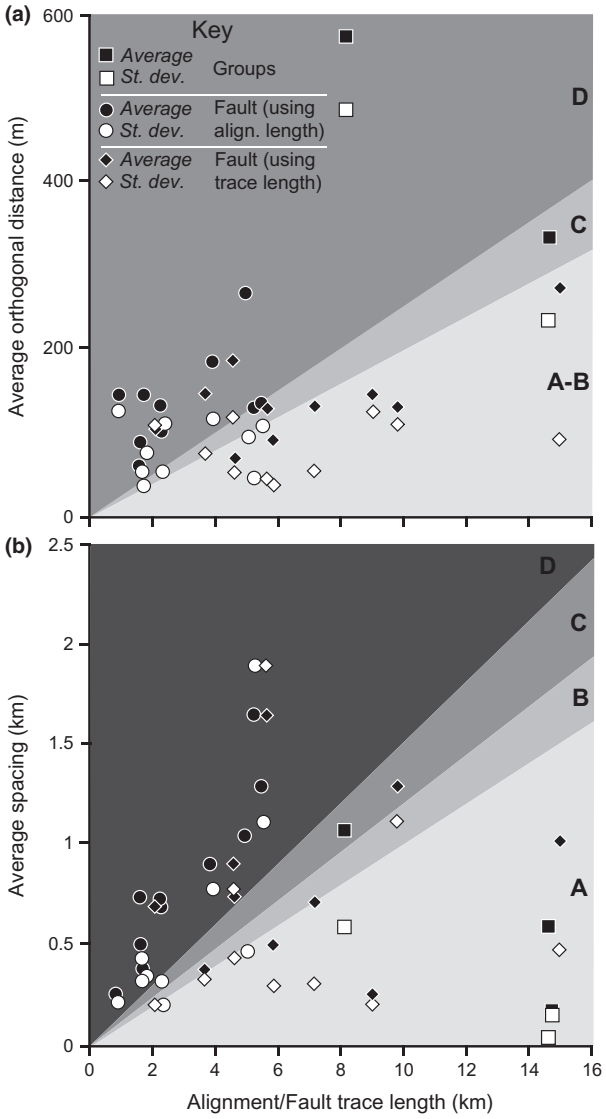

Fig. 11. Crater-hosted mound alignment or fault trace lengths plotted against average orthogonal distance (a) and average spacing (b). The greyscale areas correspond to reliability grades of 'A–D'.

that the craters developed via destructive, erosional processes at the palaeo-seabed during the early to middle Tithonian. It is likely that mound growth occurred immediately after crater formation because: (i) observed internal reflections are oriented sub-parallel to the intra-Tithonian horizon and downlap onto the base crater horizon (e.g., Fig. 7a), consistent with progressive mound growth (see Magee *et al.*, 2013b); (ii) infilling by background sedimentation processes would probably not produce the relief observed along the intra-Tithonian horizon and (iii) overlying reflections onlapping onto the mounds indicate their formation does not relate to differential compaction, although the presence of a few overlying low-relief antiforms (e.g., Fig. 10a) suggest that some differential compaction has occurred (Planke *et al.*, 2005; Hansen, 2006). Furthermore, we suggest that the mounds have comparable interval velocities to, and are likely to be composed of, the encasing Upper Jurassic Dingo Claystone because: (i) the acoustic impedance of the crater-hosted mounds is similar to that of the surrounding strata (e.g., Fig. 4; Hansen, 2006); and (ii) there are no observed geophysical artefacts which relate to seismic velocity perturbations beneath the crater-hosted mounds (e.g., velocity pull-ups, Jackson, 2012; Magee *et al.*, 2013b).

Comparison to similar features

The external morphology, scale and internal architecture of the crater-hosted mounds display similarities to: (i) carbonate mounds developed within pockmarks (e.g., Hovland *et al.*, 1994; Stewart, 1999; Hovland *et al.*, 2002, 2005); (ii) igneous intrusion-induced hydrothermal vents (e.g., Jamtveit *et al.*, 2004; Svensen *et al.*, 2004; Planke *et al.*, 2005; Hansen, 2006; Hansen *et al.*, 2008) and (iii) mud volcanoes (e.g., Stewart & Davies, 2006; Bonini & Mazzarini, 2010; Roberts *et al.*, 2011). Pockmarks are erosive (typically <45 m deep), crater-like features that form at the seabed in response to fluid seepage (Stewart, 1999; Hovland *et al.*, 2002, 2005; Ligtenberg, 2005), and may contain carbonate mounds (i.e. 'eyed' pockmarks; Hovland *et al.*, 2002). Some giant pockmarks, related to gas expulsion, have been described by Cole *et al.* (2000) that display similar diameter (0.5–4 km) and depth (50–200 m) characteristics as the crater-hosted mounds analysed here. Vents produced by the expulsion of overpressured fluids genetically related to either igneous activity or mud mobilization similarly consist of a basal crater, which is subsequently infilled by material expelled during associated fluid extrusion (e.g., Jamtveit *et al.*, 2004; Hansen, 2006; Svensen *et al.*, 2006; Roberts *et al.*, 2011). Mud volcanoes of a similar scale to the crater-hosted mounds described here have been observed (Bonini & Mazzarini, 2010), although they commonly occur in zones of tectonic shortening and display evidence of caldera collapse at their summit (Stewart & Davies, 2006; Roberts *et al.*, 2011). For intrusion-induced, eye-shaped hydrothermal vents composed of sedimentary material, previous studies have hypothesized that an increase in fluid overpressure around the lateral tips of igneous sills, instigated by the boiling of pore fluids and/or the release of magma-hosted fluids, eventually results in the rapid upwards expulsion of fluidized material (e.g., Svensen *et al.*, 2003; Jamtveit *et al.*, 2004; Planke *et al.*, 2005; Svensen *et al.*, 2006). This expelled fluid either ascends vertically, resulting in a sub-vertical 'chimney' of disturbance in seismic reflection data (Svensen *et al.*, 2003; Jamtveit *et al.*, 2004; Hansen, 2006; Svensen *et al.*, 2006), or exploits a pre-existing fault (Jackson, 2012; Magee *et al.*, 2013b).

The similarity in the morphology and seismic-stratigraphic relationships between these potential analogues and the crater-hosted mounds suggest that the craters formed through fluid expulsion at the palaeo-seabed (see Jamtveit *et al.*, 2004; Svensen *et al.*, 2006). Given the thickness of strata eroded from the craters, which can be

© 2015 The Authors
Basin Research © 2015 John Wiley & Sons Ltd, European Association of Geoscientists & Engineers and International Association of Sedimentologists

Table 2. Group 1–3 alignment reliability

Group/ Fault (Fault *a–j*)	Alignment length (Fault length) (m)	Alignment azimuth* (°)	No. of structures	Distance from best-fit line		Crater-hosted mound spacing		Angular deviation		Reliability grade (Fault grade)
				Average (m)	Standard deviation (m)	Average (m)	Standard deviation (m)	Average (°)	Standard deviation (°)	
1	8179	18	8	570	482	1067	577	69	16	D
2	14 775	18	82	1237	760	168	179	42	24	D
3	14 658	36	24	330	231	586	27	41	28	C
a	4963 (15 000)	–	5	269	92	1034	472	64	19	D (A)
b	1758 (3682)	–	5	144	73	380	331	44	28	D (D)
c	1629 (5871)	–	4	87	35	502	296	24	13	D (A)
d	2276 (7197)	–	4	129	52	714	305	49	31	D (A)
e	5507 (9817)	–	5	129	107	1294	1111	31	7	D (C)
f	2317	–	4	101	106	686	197	51	22	D (D)
g	3870 (4590)	–	5	184	115	895	777	35	30	D (D)
h	5239 (5649)	–	4	127	42	1648	1892	41	28	D (D)
i	1595 (4627)	–	3	64	50	736	431	37	26	D (D)
j	914 (9030)	–	4	142	123	250	204	17	7	D (A)

*Local fault strike, which commonly varied for each crater-hosted mound, was used to calculate angular deviation where applicable.

up to 264 m, it is likely that extrusion was explosive and provided the sedimentary material required for mound construction. Explosive ejection of material may also explain the presence of crater-infill material extending beyond the limits of the craters (Fig. 8d). We suggest that the crater-hosted mounds represent hydrothermal vents infilled by extruded mud because: (i) they are geometrically similar to hydrothermal vents observed both onshore and in seismic reflection data (see Jamtveit *et al.*, 2004; Hansen, 2006; Svensen *et al.*, 2006; Hansen *et al.*, 2008); (ii) their interval velocity is likely similar to the surrounding Dingo Claystone and (iii) no collapse caldera or evidence of intermittent extrusion events, in conjunction with the presence of basal craters, suggests that the crater-hosted mounds do not represent typical mud volcanoes (e.g., Stewart & Davies, 2006; Huuse *et al.*, 2010). We rule out a relationship between the crater-hosted mounds and pockmark formation because: (i) pockmarks rarely display crater depths >45 m (Hovland *et al.*, 2002), whereas the crater-hosted mounds are up to *c*. 264 m deep; (ii) hydrocarbon maturation and charge initiated in the Cretaceous (Tindale *et al.*, 1998) after the formation of the crater-hosted mounds, dismissing gas expulsion as a viable mechanism of giant pockmark formation (cf. Cole *et al.*, 2000) and (iii) carbonate mounds found within pockmarks have widths less than that of the host crater (Hovland *et al.*, 1994, 2002). Thus, the crater-hosted mounds are henceforth referred to as hydrothermal vents.

ORIGIN OF THE HYDROTHERMAL VENTS

Having established that the crater-hosted mounds are likely hydrothermal vents, it is perhaps appealing to link their origin to the emplacement of the underlying igneous sills observed in the seismic survey (see Jamtveit *et al.*, 2004; Hansen, 2006; Svensen *et al.*, 2006). However, Fig. 10a reveals that the majority of the vents are not spatially related to the mapped sills, as is typically expected for intrusion-induced hydrothermal vents (Jamtveit *et al.*, 2004; Hansen, 2006; Svensen *et al.*, 2006; Hansen *et al.*, 2008; Jackson, 2012; Magee *et al.*, 2014a). An igneous-related origin for the hydrothermal fluid may be maintained if it is considered that either: (1) the majority of the vents overlie dykes that are not resolved in the seismic reflection data, owing to their sub-vertical attitude (Thomson, 2005) or (2) the contemporaneous fault network allowed fluid to migrate away from a source located beneath or adjacent to the study area. Testing these two hypotheses requires elucidating the relative ages of the vents, igneous intrusions and faults. From these age relationships, the tectonic architecture contemporaneous to the emplacement of the hydrothermal vents can be reconstructed.

Timing of faulting

Onlap onto the mound flanks and truncation of the strata by the craters indicate that the hydrothermal vents formed at the palaeo-seabed (JT) during the early to middle Tithonian. Determining the architecture of the fault array at the time of vent formation requires an understanding of fault kinematic histories. To achieve this, 14 faults (Faults 1–14; Fig. 10) covering a broad range of fault sizes, orientations and geographic locations were selected for fault throw analysis. We examine fault throw variations with depth (*T*-*z*), although to aid in data comparison of faults across different depth ranges we plot

© 2015 The Authors
Basin Research © 2015 John Wiley & Sons Ltd, European Association of Geoscientists & Engineers and International Association of Sedimentologists

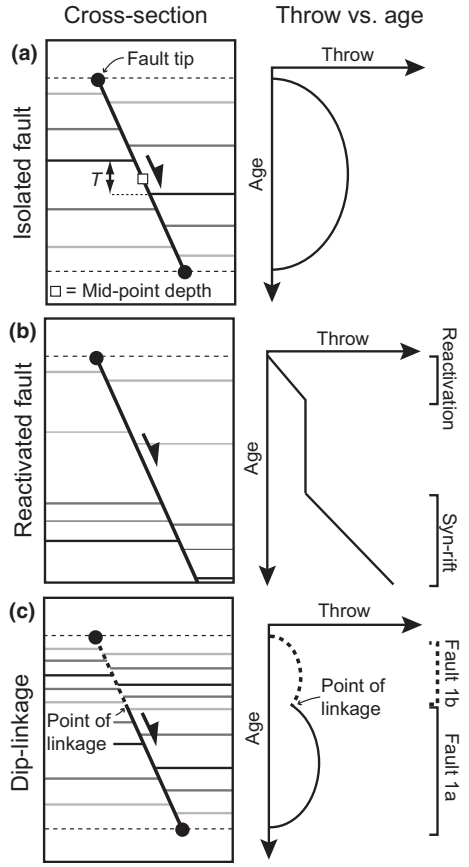

Fig. 12. Schematic diagrams showing how isolated fault growth (a), fault reactivation (b) and dip-linkage (c) are expressed on plots of throw against depth or stratigraphic age (see Muraoka & Kamata, 1983; Mansfield & Cartwright, 1996; Baudon & Cartwright, 2008; Jackson & Rotevatn, 2013; Tvedt *et al.*, 2013).

fault throw against the age (*T*-*a*) of the offset horizon, to quantify fault growth histories (e.g., Mansfield & Cartwright, 1996; Castelltort *et al.*, 2004; Hongxing & Anderson, 2007; Baudon & Cartwright, 2008; Jackson & Rotevatn, 2013). The morphology of both *T*-*z* and *T*-*a* profiles may reflect: (i) continued growth of a single, unconstrained fault that does not breach the surface (i.e. a 'C-shaped' profile geometry; Fig. 12a) (Muraoka & Kamata, 1983); (ii) reactivation of a fault (i.e. a 'stepped' profile geometry; Fig. 12b) (Hongxing & Anderson, 2007) or (iii) dip-linkage between two originally separate faults, which nucleated at different stratigraphic levels (i.e. a 'B-shaped' profile geometry; Fig. 12c) (cf. Jackson & Rotevatn, 2013; Tvedt *et al.*, 2013).

To construct the *T*-*a* profiles, throw was measured between the footwall and hanging wall cut-offs of the eleven major horizons (if present) and numerous, locally defined horizons (Fig. 12a), from seismic sections oriented orthogonal to Faults 1–14 (Fig. 10b). Where seismic reflections adjacent to the faults display evidence for significant amounts of folding, the regional trend of the horizons were extrapolated to produce footwall and hanging wall cut-offs that account for the ductile deformation (e.g., Mansfield & Cartwright, 1996; Long & Imber, 2010; Whipp *et al.*, 2014).

Within the 'pre-rift' and 'syn-rift I' successions, the *T*-*a* profiles of five vertically extensive faults indicate that fault throw decreases from *c.* >370 m near the Top Triassic (TRR) to *c.* <100 m at the base Oxfordian (JO) (Fig 13a–e). Between the base Oxfordian and intra-Tithonian (JT) horizons, which encapsulates the majority of the 'post-rift I' succession (Figs 1b, 2 and 4), generally throw remains constant, as shown by a sub-vertical slope (Fig. 13a–e). Towards the upper tips of three vertically extensive faults (i.e. Faults 1, 3 and 4), the throw gradient increases above the intra-Tithonian horizon as throw approaches zero (Fig. 13a, c and d). Overall, the vertically extensive faults display 'stepped' *T*-*a* profiles similar to Fig. 12b.

Towards the seismically defined upper and lower tips of the nine strata-bound faults analysed, throw typically approaches minimum values of *c.* <17 m and <30 m, respectively (Fig. 14). Several abrupt increases and decreases in fault throw (black arrows on Fig. 14) are observed on five of the *T*-*a* profiles, which correspond to sub-horizontal branchlines between faults of opposing dips. These composite throw values (i.e. the throw attributable to each fault cannot be distinguished) are excluded from the characterization of the strata bound fault *T*-*a* profile geometries for simplicity. Consequently, three major profile morphologies can be discerned (Fig. 14). The profiles of Faults 6–8 display a 'C-shaped' geometry, where throw increases towards a single maximum of 62 m, 36 m and 51 m, respectively, located approximately between the crater base and intra-Tithonian horizons. In contrast, Fault 9 illustrates a prominent 'B-shaped' profile, whereby an intervening throw minimum of 20 m, occurring between the intra-Tithonian and intra-Valanginian (KV) horizons, separates two zones of increased throw (Fig. 14d). A similar pattern is observed for F10–13, although the relative decrease in throw between the intra-Tithonian and intra-Valanginian horizons is less (Fig. 14e–h). Fault 14 shows little variation in throw with depth (i.e. 'I-shaped') although there is a sharp increase in the throw gradient at the intra-Hauterivian (KH) (Fig. 14i).

Interpretation

The vertically extensive fault *T*-*a* profiles (Fig. 13) are similar to the schematic 'stepped' profile depicted in Fig. 12b (cf. Hongxing & Anderson, 2007; Baudon & Cartwright, 2008). This implies that the 'syn-rift I' faults became inactive prior to deposition of the base Oxfordian to intra-Tithonian succession but were reactivated during the early to middle Tithonian (Driscoll & Karner, 1998; Mihut & Müller, 1998). Because 'C-shaped' throw profiles are characteristic of blind fault growth (Hongxing & Anderson, 2007), for the strata-bound Faults 6–8 to nucleate between the intra-Tithonian horizon and the H2 Kimmeridgian horizon (Fig. 14a–c) it is likely that they formed during the middle or late Tithonian. This implies

© 2015 The Authors
Basin Research © 2015 John Wiley & Sons Ltd, European Association of Geoscientists & Engineers and International Association of Sedimentologists

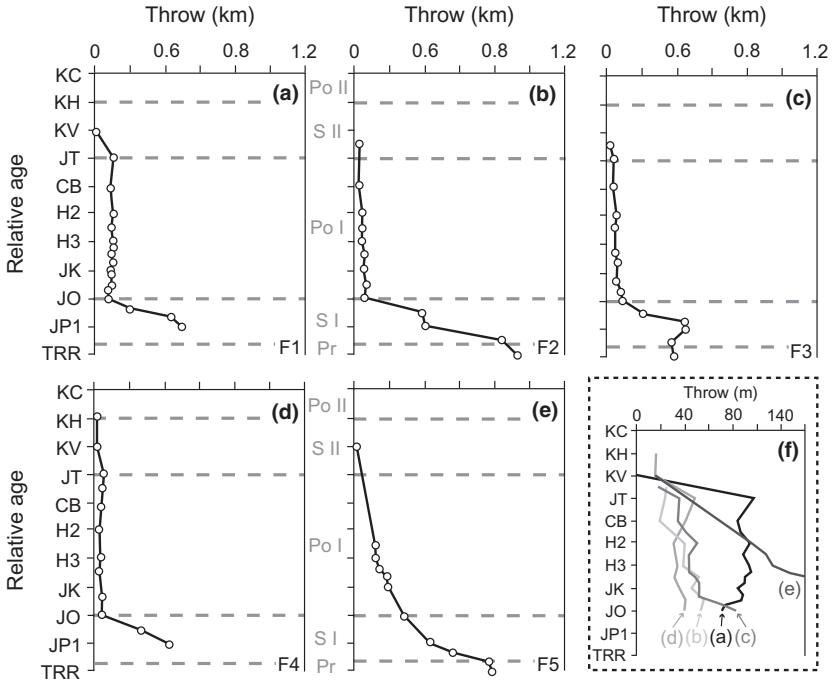

Fig. 13. (a–e) *T-a* plots for selected vertically extensive faults. Pr = 'pre-rift'; S I = 'syn-rift I'; Po I = 'post-rift I'; S II = 'syn-rift II'; Po II = 'post-rift II'. (f) Zoomed in section displaying the profile shapes above the base Oxfordian for Faults 1–F5. White circles correspond to measured horizon ages. For fault locations see Fig. 10b.

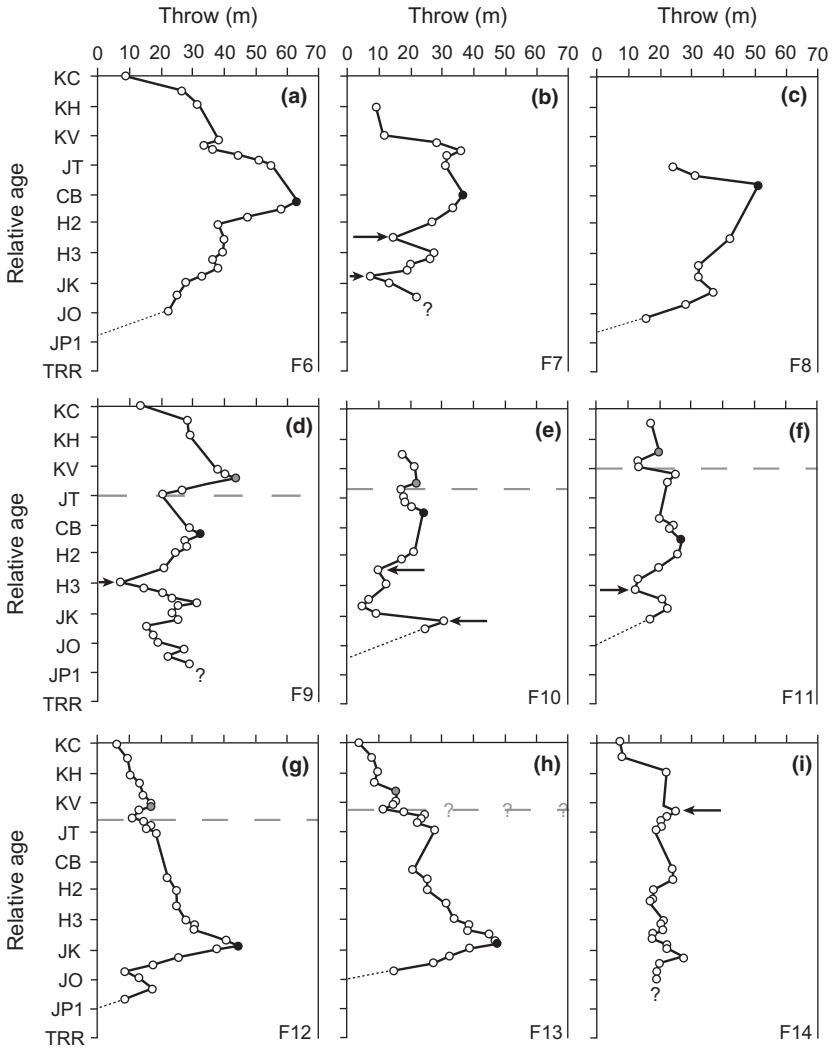

Fig. 14. (a–i) *T-a* plots for selected strata bound faults. For fault locations see Fig. 10b. White circles correspond to measured horizon ages; black (lower fault segments) and grey (lower fault segments) circles correspond to inferred nucleation points. Grey dashed lines demarcate inferred points of linkage.

© 2015 The Authors
Basin Research © 2015 John Wiley & Sons Ltd, European Association of Geoscientists & Engineers and International Association of Sedimentologists

that at least some strata-bound faults nucleated after the deposition of the intra-Tithonian horizon, and thus after the formation of the hydrothermal vents, coincident with reactivation of the 'syn-rift I' faults.

Of the nine strata-bound faults analysed, seven faults display pronounced throw minima at or just above the intra-Tithonian horizon (i.e. Fig. 14b–h). Of these faults, a further five exhibit an increase in throw above and below these minima (Fig. 14d–h), which produces a 'B-shaped' profile geometry similar to that of the dip-linked fault illustrated in Fig. 12c. Importantly, the throw maxima of these upper and lower 'segments' can be used to identify the nucleation depths of the two originally separate faults (Jackson & Rotevatn, 2013). Thus, in order to generate the *T-a* profiles observed, the shallowest fault segments must have formed after the deposition of the intra-Tithonian horizon in the middle to late Tithonian (Fig. 14), and thus after the formation of the hydrothermal vents. One explanation to account for the observed geometries is that both the upper and lower fault segments may have nucleated synchronously, becoming dip-linked with growth, which implies that strata-bound faulting postdated formation of the hydrothermal vents. Alternatively, the lower fault segments, which typically nucleated around the level of the Kimmeridgian H3–H4 horizons (Fig. 14c–h), may have formed prior to or during hydrothermal vent formation and, thus, prior to the nucleation of the upper fault segments.

Timing of magmatic activity

Four igneous sills have been mapped within the study area (Figs 1b, 7 and 10a). The timing of emplacement for seismically imaged intrusions has traditionally been constrained through radiometric dating of samples recovered from boreholes (Archer *et al.*, 2005) or the definition of horizons, with known ages, onlapping onto intrusion-induced forced folds (Trude *et al.*, 2003; Magee *et al.*, 2014a). As the sills mapped here are not associated with forced folds and are not penetrated by boreholes, we adopt the method proposed by Magee *et al.* (2013c) and determine relative emplacement ages based on their cross-cutting relationship with faults. Figure 7 reveals that sills B–D either cross-cut or are occasionally intruded along fault planes. These relationships reveal that emplacement of the imaged sills occurred after faulting ceased, likely in the Early Cretaceous (Magee *et al.*, 2013c), which is consistent with other intrusion ages suggested for the NW Australian Shelf (Mihut & Müller, 1998; McClay *et al.*, 2013; Rohrman, 2013). There is thus no genetic relationship between the sills analysed here and the Late Jurassic hydrothermal vents. However, it is important to note that Magee *et al.* (2013a) demonstrated that a saucer-shaped sill immediately to the south (*c.* 1 km) of the study area was emplaced during the mid to late Kimmeridgian (Fig. 15), prior to the formation of the hydrothermal vents. We speculate that magmatic activity on a regional-

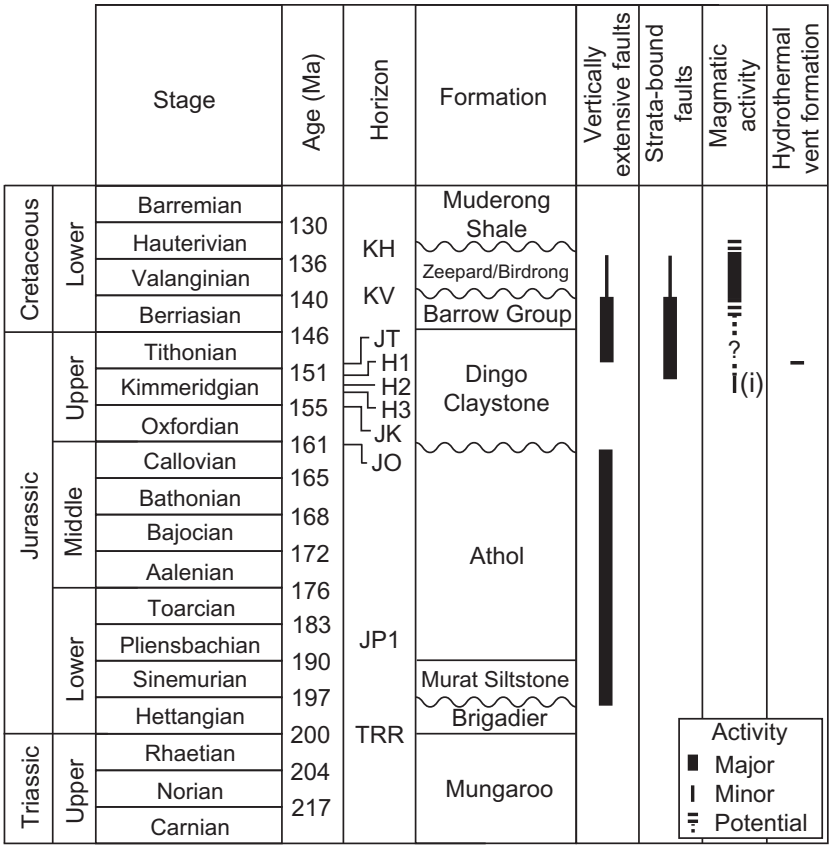

Fig. 15. Time chart detailing the constrained evolution of the study area. Magee *et al.* (2013a, 2014b) suggested that igneous activity initiated during the Kimmeridgian, before the onset of faulting.

© 2015 The Authors
Basin Research © 2015 John Wiley & Sons Ltd, European Association of Geoscientists & Engineers and International Association of Sedimentologists

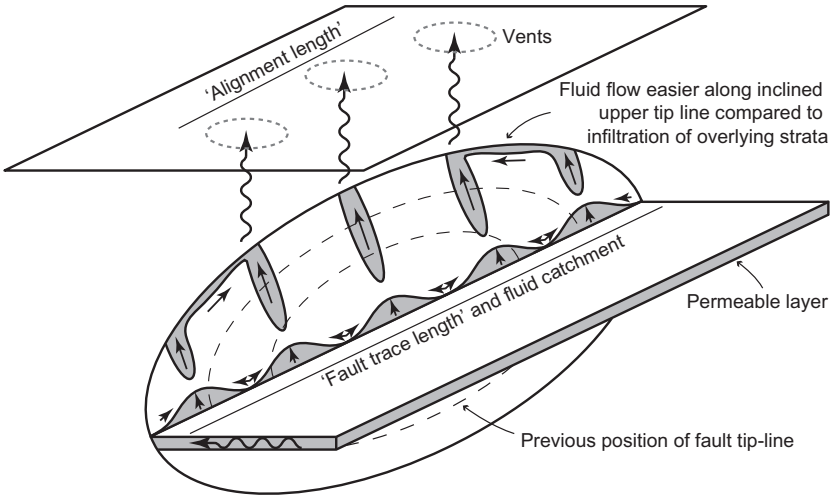

Fig. 16. Schematic diagram showing how diapiric fluid flow (after Ligtenberg, 2005) up an elliptical fault may be controlled by geometry of the upper tip line.

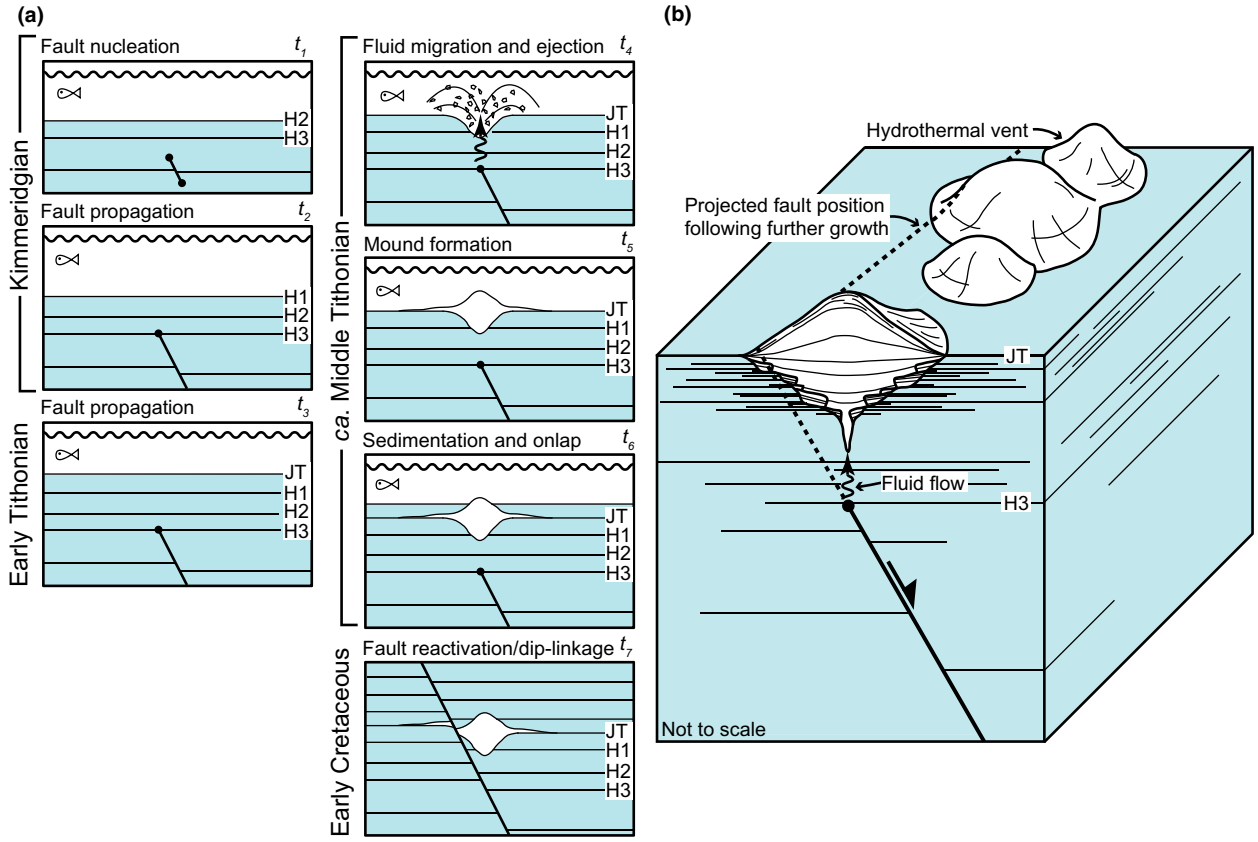

Fig. 17. (a) Schematic cartoons detailing a summarized geological history of vent formation. (b) Simplified 3D block model showing a linear alignment of hydrothermal vents situated directly above the upper tip of a blind fault. The internal structure of the vent is taken from Jamtveit *et al.* (2004) and may explain the internal reflection configuration observed.

scale initiated during the Kimmeridgian, prior to the onset of 'syn-rift II', continuing through to and intensifying during the Early Cretaceous (Fig. 15).

Vent alignment

The hydrothermal vents are organized into three broad belts (i.e. Groups 1–3), within which chains of vents apparently correlate with laterally restricted portions of fault traces along H3 defined within the Kimmeridgian succession (Fig. 10). Alignment analyses suggest that this correlation between the vents and faults can reliably be interpreted as a genetic relationship, if fluid flow occurred along the entire fault length. We consider this a reasonable assumption because: (i) Ligtenberg (2005) suggested that the ascent of fluid up fault planes draws in fluid from a zone that encompasses an area greater than the lateral limit of the surficial fluid escape structures (Fig. 16) and (ii) the upper tip-lines of normal faults typically have a convex-upwards morphology (e.g., Barnett *et al.*, 1987;

© 2015 The Authors
Basin Research © 2015 John Wiley & Sons Ltd, European Association of Geoscientists & Engineers and International Association of Sedimentologists

Walsh & Watterson, 1989), which we suggest may act to channel fluids towards the fault (segment) centre. In summary, our results indicate that it is plausible that a pre-existing network of faults captured hydrothermal fluids (e.g., Jackson, 2012; Magee *et al.*, 2013b), influencing the distribution of the hydrothermal vents during the early to middle Tithonian.

Controls on subsurface fluid flow

Reconstruction of the subsurface architecture contemporaneous to vent emplacement suggests that fluid ascended vertically from upper fault tips located around the Kimmeridgian H3 horizon (Fig. 17). This implies that the faults were blind (i.e. non-surface breaking) at this time, consistent with the lack of stratal wedges developed in the Upper Jurassic Dingo Claystone (Jitmahantakul & McClay, 2013). The difference in depth between H3 and the contemporaneous free surface (intra-Tithonian) suggests that fluid was released from the upper fault tip and ascended vertically upwards through the overlying strata before being expelled (Figs 16 and 17). This may also explain the large angular deviations >30° between the fault traces and vent long axes (Table 2) if it is considered that the far-field extensional stress regime dominated at the depth of fault nucleation, but development of the vents at the free surface was predominantly controlled by local stresses related to mechanical interaction between adjacent structures and/or variations in host rock behaviour (cf. Bonini & Mazzarini, 2010; Paulsen & Wilson, 2010). Continued fault growth after the development of the hydrothermal vents eventually resulted in the displacement of the intra-Tithonian horizon in areas adjacent to, or on the flanks of, the vents (Figs 4, 8a and 17).

There is no consistent pattern in the spacing of the hydrothermal vents relative to fault length, geometry (e.g., curvature) or intersection locations as is commonly observed when faults act as fluid flow conduits (e.g., Ligtenberg, 2005; Abebe *et al.*, 2007; Mazzarini, 2007; Paulsen & Wilson, 2010; Andresen, 2012; Magee *et al.*, 2013c). Given the complex distribution of faults at H3 (Figs 5c and 10b), we suggest that the interaction between all the aforementioned fault array properties locally influenced fluid flow. Detailed analyses of ancient fluid escape structures imaged in 3D seismic reflection data could therefore provide an important opportunity to further constrain these controls.

CONCLUSIONS

The upper crustal structure of rift basins influences fluid flow in the subsurface. Identifying the processes which control fluid distribution can therefore provide significant insights into the evolution of hydrothermal, magmatic and hydrocarbon systems. However, the interaction between fluids and structures, particularly normal faults, in the subsurface cannot be easily examined. We present a quantitative analysis of a suite of ancient hydrothermal vents imaged in 3D seismic reflection data offshore NW Australia. The vents are circular to elliptical (<3.5 km diameter) map-view and consist of a basal crater that truncates surrounding strata and infilled by a mound onlapped by overlying reflections. Associated with the hydrothermal vents are two arrays of normal faults and several igneous sills. The analysis of seismic-stratigraphic relationships and fault growth histories reveal that hydrothermal vent emplacement occurred in the early to middle Tithonian, likely after the initial onset (Kimmeridgian?) of local faulting. Although the sills imaged in the study area post-date vent formation and faulting, we suggest that the hydrothermal fluids were generated in response to regional magmatic activity. A statistical assessment of the apparent alignment of hydrothermal vents along underlying fault traces suggests that the fault architecture influenced fluid flow. We propose a model whereby the convex-upwards, upper tip-line morphology of individual faults channelled fluid towards the fault (segment) centre, localizing hydraulic failure of the overburden and hydrothermal vent distribution. We also show that fault curvature and fault intersections complicate fluid flow systems. Our results emphasize the importance of 3D seismic reflection data to understanding fluid flow in the subsurface and suggest that integrated structural analyses can be applied to reconstruct ancient fluid flow pathways.

ACKNOWLEDGEMENTS

Geoscience Australia and Schlumberger are thanked for the provision of the seismic data and interpretation software, respectively. We are grateful to Mads Huuse and Henrik Svensen for excellent reviews and to Peter van der Beek for his editorial handling.

SUPPORTING INFORMATION

Additional Supporting Information may be found in the online version of this article:

Figure S1. Uninterpreted seismic sections corresponding to Figs 7a, 7b and 9a.

REFERENCES

Abebe, B., Acocella, V., Korme, T. & Ayalew, D. (2007) Quaternary faulting and volcanism in the Main Ethiopian Rift. *J. Afr. Earth Sc.*, **48**, 115–124.

Allan, U.S. (1989) Model for hydrocarbon migration and entrapment within faulted structures. *AAPG Bull.*, **73**, 803–811.

Andresen, K.J. (2012) Fluid flow features in hydrocarbon plumbing systems: what do they tell us about the basin evolution? *Mar. Geol.*, **332–334**, 89–108.

Andresen, K.J., Clausen, O.R. & Huuse, M. (2009) A Giant (5.3× 107 M3) middle Miocene (C. 15ma) sediment mound

© 2015 The Authors
Basin Research © 2015 John Wiley & Sons Ltd, European Association of Geoscientists & Engineers and International Association of Sedimentologists

(M1) above the Siri Canyon, Norwegian-Danish basin: origin and significance. *Mar. Pet. Geol.*, **26**, 1640–1655.

Archer, S.G., Bergman, S.C., Iliffe, J., Murphy, C.M. & Thornton, M. (2005) Palaeogene igneous rocks reveal new insights into the geodynamic evolution and petroleum potential of the Rockall Trough, NE Atlantic Margin. *Basin Res.*, **17**, 171–201.

Barnett, J.A., Mortimer, J., Rippon, J.H., Walsh, J.J. & Watterson, J. (1987) Displacement geometry in the volume containing a single normal fault. *AAPG Bull.*, **71**, 925–937.

Baudon, C. & Cartwright, J. (2008) The kinematics of reactivation of normal faults using high resolution throw mapping. *J. Struct. Geol.*, **30**, 1072–1084.

Bedard, J.H., Naslund, H.R., Nabelek, P., Winpenny, A., Hryciuk, M., Macdonald, W., Hayes, B., Steigerwaldt, K., Hadlari, T., Rainbird, R., Dewing, K. & Girard, E. (2012) Fault-mediated melt ascent in a Neoproterozoic continental flood basalt province, the Franklin Sills, Victoria Island, Canada. *Geol. Soc. Am. Bull.*, **124**, 723–736.

Bonini, M. & Mazzarini, F. (2010) Mud volcanoes as potential indicators of regional stress and pressurized layer depth. *Tectonophysics*, **494**, 32–47.

Brown, A.R. (2004) *Interpretation of Three-Dimensional Seismic Data*. 6th edn. AAPG and SEG, Oklahoma, USA.

Cartwright, J., Huuse, M. & Aplin, A. (2007) Seal bypass systems. *AAPG Bull.*, **91**, 1141–1166.

Castelltort, S., Pochat, S. & Van Den Driessche, J. (2004) Using T-Z plots as a graphical method to infer Lithological variations from growth strata. *J. Struct. Geol.*, **26**, 1425–1432.

Cole, D., Stewart, S.A. & Cartwright, J.A. (2000) Giant irregular pockmark craters in the Palaeogene of the outer moray Firth Basin, UK North Sea. *Mar. Pet. Geol.*, **17**, 563–577.

Driscoll, N.W. & Karner, G.D. (1998) Lower crustal extension across the Northern Carnarvon basin, Australia: evidence for an eastward dipping detachment. *J. Geophys. Res.*: Solid Earth (1978–2012), **103**, 4975–4991.

Egger, A.E., Glen, J.M.G. & McPhee, D.K. (2014) Structural controls on geothermal circulation in Surprise Valley, California: a re-evaluation of the Lake City Fault Zone. *Geol. Soc. Am. Bull.*, **126**, 523–531.

Gaffney, E.S., Damjanac, B. & Valentine, G.A. (2007) Localization of volcanic activity: 2. Effects of pre-existing structure. *Earth Planet. Sci. Lett.*, **263**, 323–338.

Giordano, G., Pinton, A., Cianfarra, P., Baez, W., Chiodi, A., Viramonte, J., Norini, G. & Groppelli, G. (2013) Structural control on geothermal circulation in the Cerro Tuzgle-Tocomar geothermal volcanic area (Puna Plateau, Argentina). *J. Volcanol. Geoth. Res.*, **249**, 77–94.

Groves, D.I. & Bierlein, F.P. (2007) Geodynamic settings of mineral deposit systems. *J. Geol. Soc.*, **164**, 19–30.

Hamilton, E.L. (1985) Sound velocity as a function of depth in marine sediments. *J. Acoust. Soc. Am.*, **78**, 1348–1355.

Hamilton, E.L., Bachman, R.T., Curray, J.R. & Moore, D.G. (1977) Sediment velocities from sonobuoys: Bengal Fan, Sunda Trench, Andaman Basin, and Nicobar Fan. *J. Geophys. Res.*, **82**, 3003–3012.

Hansen, D.M. (2006) The morphology of intrusion-related vent structures and their implications for constraining the timing of intrusive events along the NE Atlantic Margin. *J. Geol. Soc.*, **163**, 789–800.

Hansen, J.P.V., Cartwright, J.A., Huuse, M. & Clausen, O.R. (2005) 3D seismic expression of fluid migration and mud remobilization on the Gjallar Ridge, Offshore Mid-Norway. *Basin Res.*, **17**, 123–139.

Hansen, D.M., Redfern, J., Federici, F., di Biase, D. & Bertozzi, G. (2008) Miocene igneous activity in the Northern Subbasin, offshore Senegal, NW Africa. *Mar. Pet. Geol.*, **25**, 1–15.

Holford, S.P., Schofield, N., MacDonald, J.D., Duddy, I.R. & Green, P.F. (2012) Seismic analysis of igneous systems in sedimentary basins and their impacts on hydrocarbon prospectivity: examples from the Southern Australian Margin. *APPEA J.*, **52**, 23.

Hongxing, G. & Anderson, J.K. (2007) Fault Throw profile and Kinetmatics of Normal Fault: conceptual Models and Geologic Examples. *Geol. J. China Univ.*, **13**, 13.

Hovland, M., Croker, P.F. & Martin, M. (1994) Fault-associated seabed mounds (carbonate knolls?) off western Ireland and north-west Australia. *Mar. Pet. Geol.*, **11**, 14.

Hovland, M., Gardner, J. & Judd, A. (2002) The significance of pockmarks to understanding fluid flow processes and geohazards. *Geofluids*, **2**, 127–136.

Hovland, M., Svensen, H., Forsberg, C.F., Johansen, H., Fichler, C., Fosså, J.H., Jonsson, R. & Rueslåtten, H. (2005) Complex pockmarks with carbonate-ridges off mid-Norway: products of sediment degassing. *Mar. Geol.*, **218**, 191–206.

Huuse, M., Jackson, C.A.L., Van Rensbergen, P., Davies, R.J., Flemings, P.B. & Dixon, R.J. (2010) Subsurface sediment remobilization and fluid flow in sedimentary basins: an overview. *Basin Res.*, **22**, 342–360.

Isola, I., Mazzarini, F., Bonini, M. & Corti, G. (2014) Spatial variability of volcanic features in early-stage rift settings: the case of the Tanzania Divergence, East African rift system. *Terra Nova*, **26**, 461–468.

Jackson, C.A.-L. (2012) Seismic reflection imaging and controls on the preservation of ancient sill-fed magmatic vents. *J. Geol. Soc.*, **169**, 503–506.

Jackson, C.A.L. & Rotevatn, A. (2013) 3D seismic analysis of the structure and evolution of a salt-influenced normal fault zone: a test of competing fault growth models. *J. Struct. Geol.*, **54**, 215.

Jamtveit, B., Svensen, H., Podladchikov, Y.Y. & Planke, S. (2004) Hydrothermal vent complexes associated with sill intrusions in sedimentary basins. *Phys. Geol. High-level Magn. Syst.*, **234**, 233–241.

Jitmahantakul, S. & McClay, K. (2013) Late Triassic - Mid-Jurassic to Neogene Extensional Fault Systems in the Exmouth Sub-Basin, Northern Carnarvon Basin, North West Shelf, Western Australia. (Ed. by M. Keep & S. J. Moss). The Sedimentary Basins of Western Australia IV: Proceedings of the Petroleum Exploration Society of Australia Symposium, Perth, WA, 2013.

Le Corvec, N., Spörli, K.B., Rowland, J. & Lindsay, J. (2013) Spatial distribution and alignments of volcanic centers: clues to the formation of monogenetic volcanic fields. *Earth Sci. Rev.*, **124**, 96–114.

Ligtenberg, J.H. (2005) Detection of fluid migration pathways in seismic data: implications for fault seal analysis. *Basin Res.*, **17**, 141–153.

Long, J.J. & Imber, J. (2010) Geometrically coherent continuous deformation in the volume surrounding a seismically imaged normal fault-array. *J. Struct. Geol.*, **32**, 222–234.

© 2015 The Authors
Basin Research © 2015 John Wiley & Sons Ltd, European Association of Geoscientists & Engineers and International Association of Sedimentologists

Magee, C., Briggs, F. & Jackson, C.A.-L. (2013a) Lithological controls on igneous intrusion-induced ground deformation. *J. Geol. Soc.*, **170**, 853–856.

Magee, C., Hunt-Stewart, E. & Jackson, C.A.L. (2013b) Volcano growth mechanisms and the role of sub-volcanic intrusions: insights from 2D seismic reflection data. *Earth Planet. Sci. Lett.*, **373**, 41–53.

Magee, C., Jackson, C.A.-L. & Schofield, N. (2013c) The influence of normal fault geometry on igneous sill emplacement and morphology. *Geology*, **41**, 407–410.

Magee, C., Jackson, C.L. & Schofield, N. (2014a) Diachronous sub-volcanic intrusion along deep-water margins: insights from the Irish Rockall Basin. *Basin Res.*, **26**, 85–105.

Magee, C., McDermott, K.G., Stevenson, C.T. & Jackson, C.A.-L. (2014b) Influence of crystallised igneous intrusions on fault nucleation and reactivation during continental extension. *J. Struct. Geol.*, **62**, 183–193.

Mansfield, C.S. & Cartwright, J.A. (1996) High resolution fault displacement mapping from three-dimensional seismic data: evidence for dip linkage during fault growth. *J. Struct. Geol.*, **18**, 14.

Mazzarini, F. (2007) Vent distribution and crustal thickness in stretched continental crust: the case of the Afar Depression (Ethiopia). *Geosphere*, **3**, 152–162.

McClay, K., Scarselli, N. & Jitmahantakul, S. (2013) Igneous Intrusions in the Carnarvon Basin, NW Shelf, Australia. In: *The Sedimentary Basins of Western Australia IV* (Ed. by M. Keep, S.J. Moss), Proceedings of the Petroleum Exploration Society of Australia Symposium, Perth, WA, 20pp.

Mihut, D. & Müller, R.D. (1998) Volcanic margin formation and Mesozoic rift propagators in the Cuvier Abyssal Plain off Western Australia. *J. Geophys. Res.*, **103**, 27135–27149.

Muraoka, H. & Kamata, H. (1983) Displacement distribution along minor fault traces. *J. Struct. Geol.*, **5**, 483–495.

Paulsen, T.S. & Wilson, T.J. (2010) New criteria for systematic mapping and reliability assessment of monogenetic volcanic vent alignments and elongate volcanic vents for crustal stress analyses. *Tectonophysics*, **482**, 16–28.

Planke, S., Rasmussen, T., Rey, S.S. & Myklebust, R. (2005) Seismic characteristics and distribution of volcanic intrusions and hydrothermal vent complexes in the Vøring and Møre Basins. In: *Petroleum Geology: North-West Europe and Global Perspectives - Proceddings of the 6th Petroleum Geology Conference* (Ed. by A.G. Doré), pp. 833–844. Geological Society, London.

Rasband, W.S. (1997) *Imagej*. US National Institutes of Health, Bethesda, MD, USA.

Rey, S.S., Planke, S., Symonds, P.A. & Faleide, J.I. (2008) Seismic volcanostratigraphy of the Gascoyne margin, Western Australia. *J. Volcanol. Geoth. Res.*, **172**, 112–131.

Roberts, K.S., Davies, R.J., Stewart, S.A. & Tingay, M. (2011) Structural controls on mud volcano vent distributions: examples from Azerbaijan and Lusi, East Java. *J. Geol. Soc.*, **168**, 1013–1030.

Rohrman, M. (2013) Intrusive large igneous provinces below sedimentary basins: an example from the Exmouth Plateau (NW Australia). *J. Geophys. Res.*: Solid Earth, **118**, 4477–4487.

Skogly, O. (1998) Seismic Characterization and Emplacement of Intrusives in the Vøring Basin. M.Sc. Thesis Thesis, University of Oslo.

Smallwood, J.R. & Maresh, J. (2002) The Properties, Morphology and Distribution of Igneous Sills: modelling, Borehole Data and 3D Seismic from the Faroe-Shetland Area. In: *The North Atlantic Igneous Province: Stratigraphy, Tectonic, Volcanic and Magmatic Processes* (Ed. by D.W. Jolley & B.R. Bell), 197, pp. 271–306. Geological Society, London, Special Publications.

Stewart, S.A. (1999) Seismic interpretation of circular geological structures. *Petrol. Geosci.*, **5**, 12.

Stewart, S.A. & Davies, R.J. (2006) Structure and emplacement of mud volcano systems in the South Caspian Basin. *AAPG Bull.*, **90**, 771–786.

Svensen, H., Planke, S., Jamtveit, B. & Pedersen, T. (2003) Seep carbonate formation controlled by hydrothermal vent complexes: a case study from the Vøring Basin, the Norwegian Sea. *Geo-Mar. Lett.*, **23**, 351–358.

Svensen, H., Planke, S., Malthe-Sorenssen, A., Jamtveit, B., Myklebust, R., Rasmussen Eidem, T. & Rey, S.S. (2004) Release of methane from a volcanic basin as a mechanism for initial eocene global warming. *Nature*, **429**, 542–545.

Svensen, H., Jamtveit, B., Planke, S. & Chevallier, L. (2006) Structure and evolution of hydrothermal vent complexes in the Karoo Basin, South Africa. *J. Geol. Soc.*, **163**, 11.

Symonds, P.A., Planke, S., Frey, O. & Skogseid, J. (1998) Volcanic Evolution of the Western Australian Continental Margin and Its Implications for Basin Development. The Sedimentary Basins of Western Australia 2: Proc. of Petroleum Society Australia Symposium, Perth, WA.

Thomson, K. (2005) Volcanic features of the North Rockall Trough: application of visualisation techniques on 3D seismic reflection data. *Bull. Volcanol.*, **67**, 116–128.

Tindale, K., Newell, N., Keall, J. & Smith, N. (1998). *Structural Evolution and Charge History of the Exmouth Sub-Basin, Northern Carnarvon Basin, Western Australia*. The Sedimentary Basins of Western Australia 2: Proc. of Petroleum Society Australia Symposium, Perth, WA.

Trude, J., Cartwright, J., Davies, R.J. & Smallwood, J.R. (2003) New technique for dating igneous sills. *Geology*, **31**, 4.

Tvedt, A., Rotevatn, A., Jackson, C.A.-L., Fossen, H. & Gawthorpe, R.L. (2013) Growth of normal faults in multilayer sequences: A 3D seismic case study from the Egersund Basin, Norwegian North Sea. *J. Struct. Geol.*, **55**, 1–20.

Valentine, G. & Krogh, K. (2006) Emplacement of shallow dikes and sills beneath a small basaltic volcanic center – the role of pre-existing structure (Paiute Ridge, Southern Nevada, USA). *Earth Planet. Sci. Lett.*, **246**, 217–230.

Walsh, J.J. & Watterson, J. (1989) Displacement gradients on fault surfaces. *J. Struct. Geol.*, **11**, 307–316.

Walsh, J., Watterson, J., Heath, A. & Childs, C. (1998) Representation and scaling of faults in fluid flow models. *Petrol. Geosci.*, **4**, 241–251.

Whipp, P.S., Jackson, C.A.L., Gawthorpe, R.L., Dreyer, T. & Quinn, D. (2014) Normal fault array evolution above a reactivated rift fabric; a subsurface example from the Northern Horda Platform, Norwegian North Sea. *Basin Res.*, **26**, 523–549.

Yielding, G., Freeman, B. & Needham, D.T. (1997) Quantitative fault seal prediction. *AAPG Bull.*, **81**, 897–917.

Manuscript received 6 June 2014; In revised form 20 November 2014; Manuscript accepted 3 December 2014.

© 2015 The Authors
Basin Research © 2015 John Wiley & Sons Ltd, European Association of Geoscientists & Engineers and International Association of Sedimentologists